

**Analytic bond-order potential for the gallium arsenide system**

D. A. Murdick,\* X. W. Zhou, and H. N. G. Wadley

*Department of Materials Science and Engineering, School of Engineering and Applied Science, University of Virginia, Charlottesville, Virginia 22904, USA*

D. Nguyen-Manh

*UKAEA Culham Division, Culham Science Centre, Abingdon, OX14 3DB, United Kingdom*

R. Drautz and D. G. Pettifor

*Department of Materials, University of Oxford, Oxford OX1 3PH, United Kingdom*

(Received 24 October 2005; published 20 January 2006)

An analytic, bond-order potential (BOP) is proposed and parametrized for the gallium arsenide system. The potential addresses primary ( $\sigma$ ) and secondary ( $\pi$ ) bonding and the valence-dependent character of heteroatomic bonding, and it can be combined with an electron counting potential to address the distribution of electrons on the GaAs surface. The potential was derived from a tight-binding description of covalent bonding by retaining the first two levels of an expanded Green's function for the  $\sigma$  and  $\pi$  bond-order terms. Predictions using the potential were compared with independent estimates for the structures and binding energy of small clusters (dimers, trimers, and tetramers) and for various bulk lattices with coordinations varying from 4 to 12. The structure and energies of simple point defects and melting transitions were also investigated. The relative stabilities of the (001) surface reconstructions of GaAs were well predicted, especially under high-arsenic-overpressure conditions. The structural and binding energy trends of this GaAs BOP generally match experimental observations and *ab initio* calculations.

DOI: [10.1103/PhysRevB.73.045206](https://doi.org/10.1103/PhysRevB.73.045206)

PACS number(s): 61.50.Ah, 81.05.Ea, 61.50.Lt

**I. INTRODUCTION**

The vapor phase growth of gallium arsenide thin films is an area of significant technological interest and study.<sup>1</sup> Nonetheless, uncertainties remain about the atomic-scale assembly phenomena active during GaAs thin-film growth.<sup>2–11</sup> In principle, these molecular assembly mechanisms can be studied with molecular dynamics (MD).<sup>12</sup> In other material systems,<sup>13–16</sup> MD simulations enable atom coordinates to be tracked with femtosecond time resolution for many nanoseconds in response to realistically modeled interatomic forces. As a result, they provide information about vapor impact dynamics, transient surface structures, and defect formation mechanisms during growth. The deposition time that can be simulated depends on the complexity of the interatomic potential, its interaction distance (cutoff length), the number of atoms simulated, and the available computing resources. In general, analytic potentials enable tens to hundreds of nanoseconds of simulation for computational systems involving thousands of atoms using desktop computing resources. However, the validity of the results is highly dependent upon the fidelity with which interatomic forces are modeled by the potential.

The usual approach to the development of an interatomic potential involves fitting a physically motivated potential energy function to a database of physical properties for the system of interest. A large experimental<sup>1,17,18</sup> and *ab initio*<sup>19–22</sup> database is available to guide the fitting and evaluation of potentials for the GaAs system. However, the validity of the angular and radially dependent forces between the atoms can be limited by both their functional representation by the potential and by inaccuracies introduced during

parametrization.<sup>23</sup> High fidelity is especially important during simulations of vapor deposition, where the local atomic environment radically changes over short periods of time. Currently, the best GaAs interatomic potentials either predict unrealistically weak As-As dimer bonds or significantly underestimate the As<sub>2</sub> molecule sticking probability upon impact with the GaAs (001) surface.<sup>23</sup> These shortcomings significantly restrict the problems that previously parametrized empirical potentials can satisfactorily analyze.<sup>12</sup>

Bond-order potentials (BOP's) seek to overcome some of the limitations of empirical potentials by formally coarse-graining and linking the electronic structure inherent in a tight-binding approximation to atomic bonding.<sup>24</sup> The functional form of the resulting analytic potential has been derived and fully justified for *sp*-valent systems.<sup>25</sup> The BOP formalism includes separate contributions from molecular orbitals describing both  $\sigma$ - and  $\pi$ -type bonds<sup>26</sup> and can be applied to open phase (half-full valence shell) materials, close-packed structures,<sup>27</sup> and compound phases.<sup>28</sup> Recently, the BOP approach has been generalized to more effectively model *sp*-valent elements in material systems where the degree of valence shell filling is incorporated.<sup>29</sup> In principle, this band-filling functionality enables the modeling of elements across the periodic table.

Here, we propose an analytic BOP for the GaAs system and deduce the parameters that define it. The potential is used to predict bulk lattice parameters, cohesive energies, and elastic properties of the elemental and compound phases, various point-defect formation energies, and the (001) surface free energies of the zinc-blende (zb) GaAs structure. These are then compared with independent observations and used to assess the potential's suitability for simulations of the

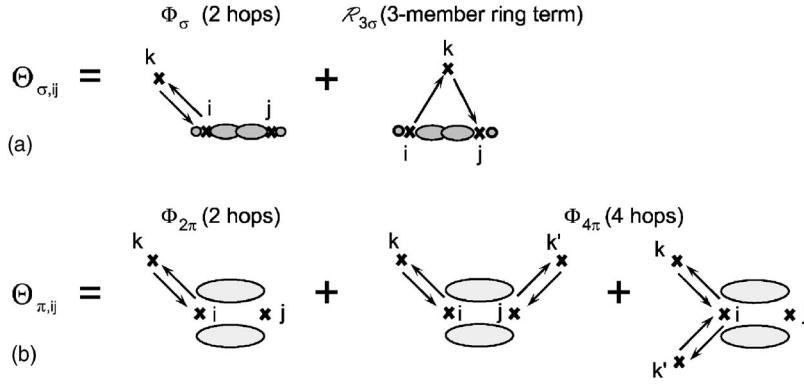


FIG. 1. A schematic representation of the hopping paths that sample the local atomic configuration (atoms  $k$  and  $k'$ ) around the  $ij$  bond (atoms  $i$  and  $j$ ), forming a bond. The hopping paths of a primary  $\sigma$  covalent bond are shown in (a) and expressed in Eqs. (9) and (12). The hopping paths of secondary  $\pi$  covalent bonds are shown in (b) and expressed by Eqs. (19) and (22).

homoepitaxial growth of GaAs. Requiring a potential to represent interactions for a wide range of environmental configurations has proven to be challenging.<sup>23</sup> The potential proposed here is shown to be a significant step toward this goal.

## II. BOND-ORDER POTENTIAL

### A. Potential format

We seek a potential energy function that reliably represents the radial and angular dependence of the dynamic interatomic forces as atoms and molecules break and reform bonds during the assembly of a condensed GaAs structure. The homoatomic and heteroatomic bonding within the condensed phases of gallium, arsenic, and GaAs involves  $sp$  hybridization of the overlapping molecular orbitals. The bond order (defined as one-half the difference between the number of bonding and antibonding electrons in the molecular orbitals between adjacent atoms<sup>30</sup>) provides a foundation for quantifying bond strength. Bond orders, when multiplied by bond (hopping) integrals, yield bonding energies.<sup>31</sup> The bond integrals in turn are related to the probability that an electron will hop from one molecular orbital to another and therefore depend on nearest-neighbor distance and orbital type.<sup>32</sup> The derivation of a general analytic expression for the reduced (the separated  $\sigma$  and  $\pi$  bond-order terms) BOP from two-center, orthogonal tight-binding theory has been detailed by Pettifor and his collaborators.<sup>25–27,33</sup>

A potential energy function ( $E$ ) can be expressed as the sum of bonding ( $U_{\text{bond}}$ ) and repulsive ( $U_{\text{rep}}$ ) energy terms:

$$E = U_{\text{bond}} + U_{\text{rep}}, \quad (1)$$

where the  $sp$  hybridization promotion energy term<sup>28</sup> has been grouped with  $U_{\text{rep}}$  to form a single repulsive energy term, simplifying the parametrization process discussed later.

Consider a system of widely separated arsenic and gallium atoms in the vapor that are allowed to condense. Atom  $i$  can form bonds ( $ij$ ) with its  $j$  neighbors. These bonds can have  $\sigma$  (primary covalent) and  $\pi$  (secondary covalent) bonding character. The bonding energy term in Eq. (1) for such a system is found by summing the product of the bond order and bond integral for each bond over all  $ij$  bonds for both the  $\sigma$  and  $\pi$  bond energy terms. This can be written

$$U_{\text{bond}} = -\frac{1}{2} \sum_i \sum_{j, j \neq i} [2\beta_{\sigma,ij} \Theta_{\sigma,ij} + 2\beta_{\pi,ij} \Theta_{\pi,ij}], \quad (2)$$

where  $\beta_{\sigma,ij}$  and  $\beta_{\pi,ij}$  are the  $\sigma$  and  $\pi$  bond integrals between atoms  $i$  and  $j$ ,  $\Theta_{\sigma,ij}$  is the  $\sigma$  bond-order term, and  $\Theta_{\pi,ij}$  is the  $\pi$  bond-order term.<sup>34</sup> The bond integrals are functions of the interatomic distance ( $r_{ij}$ ) between atoms  $i$  and  $j$ . The bond orders are scalar quantities that are dependent on the local atomic environment in the vicinity of the  $ij$  bond.<sup>25</sup> The maximum value of the  $\sigma$  bond order ( $\Theta_{\sigma,ij}$ ) is 1, while that of the  $\pi$  bond order ( $\Theta_{\pi,ij}$ ) is 2. For  $sp$  systems, the total bond order ( $\Theta_{\sigma} + \Theta_{\pi}$ ) therefore has a maximum value of 3. The  $\sigma$  and  $\pi$  bond orders reflect the ubiquitous single-, double-, and triple-bond behavior of chemistry.

The bond orders can be related to an intersite Green's function,<sup>25,26</sup> which can be expanded as a continued fraction by using the Lanczos recursion algorithm<sup>35,36</sup> to obtain  $\Theta_{\sigma}$  and by using matrix recursion to obtain  $\Theta_{\pi}$ .<sup>37,38</sup> Here we retain two levels of the recursive representations for both the  $\sigma$  and  $\pi$  bond contributions. The resulting two-level potential is a compromise that results in a computationally efficient potential formulation suitable for MD simulations, while retaining sufficient terms to capture the most significant aspects of bonding in the GaAs system.

During derivation of the bond-order terms, the expansion of the intersite Green's function produces coefficients that can be directly related to molecular orbital hopping paths via the Cyrot-Lackmann theorem.<sup>25</sup> The  $n$ th moment of the electronic eigenspectrum is directly related to hopping paths of length  $n$  around the bond.<sup>39</sup> The hopping paths sample the local atomic configuration and are dependent on bond length and three- and four-body (dihedral) angles. Many possible hopping paths through molecular orbitals between atoms  $i$  and  $j$  and the surrounding atoms exist. The two-level  $\sigma$  bond order has hopping paths of length 2 and is therefore a second moment approximation to the density of states<sup>25</sup> (DOS); the  $\pi$  bond order has hopping paths of length 4 and is a fourth moment approximation to the DOS.<sup>26</sup> The hopping paths utilized in this work are shown in Fig. 1.

The  $\sigma$  and  $\pi$  bond hopping integrals have a common functional form and can be written as

$$\beta_{\sigma} = \beta_{\sigma,0} f(r)^n, \quad (3)$$

$$\beta_\pi = \beta_{\pi,0} f(r)^n, \quad (4)$$

where  $f(r)$  is a radially dependent Goodwin-Skinner-Pettifor<sup>34</sup> (GSP) function (described later),  $\beta_{\sigma,0}$  and  $\beta_{\pi,0}$  are prefactors that determine the magnitude of the bond energy for the  $\sigma$  and  $\pi$  bonds, and  $n$  is an exponent that controls how quickly  $\beta_\sigma$  and  $\beta_\pi$  approach zero as the interatom distance  $r$  increases.

The repulsive component of the BOP uses a short-range two-body GSP function  $\phi_{ij}$  to approximate repulsion between a pair of ion cores. It also incorporates the electron Coulomb repulsion and the energy required to promote  $s$  and  $p$  electrons to  $sp^3$  hybrid atomic orbitals.<sup>28,40</sup> The repulsive potential energy between atoms  $i$  and  $j$  can then be written as the sum of two-body functions that depend upon only the interatomic separation distance:

$$U_{\text{rep}} = \frac{1}{2} \sum_i \sum_{j \neq i} \phi_{ij}, \quad (5)$$

where

$$\phi = \phi_0 f(r)^m. \quad (6)$$

The prefactor  $\phi_0$  represents the magnitude of the repulsive energy, and  $m$  is an exponent that controls the repulsive energy gradient as the interatomic spacing is changed.

The GSP function identified in Eqs. (3), (4), and (6) has the form<sup>34</sup>

$$f(r) = \frac{r_0}{r} \exp \left[ \left( \frac{r_0}{r_c} \right)^{n_c} - \left( \frac{r}{r_c} \right)^{n_c} \right], \quad (7)$$

where  $r$  is the interatomic spacing between a pair of atoms,  $r_0$  is the interatomic spacing at which  $f(r_0)=1$ ,  $r_c$  is a characteristic radius, and  $n_c$  is a characteristic exponent. The pair function parameters, including prefactors ( $\phi_0$ ,  $\beta_{\sigma,0}$ , and  $\beta_{\pi,0}$ ), exponents ( $m$ ,  $n$ , and  $n_c$ ), and radii ( $r_0$  and  $r_c$ ), each depend on the elemental type of atoms  $i$  and  $j$  that participate in the two-body interactions. We have assumed that the  $r_0$ ,  $r_c$ , and  $n_c$  parameters have identical values for the three two-body functions in Eqs. (3), (4), and (6). It is a simple generalization to lift this constraint. However, we found that this generalized form did not improve the potential's performance or its ease of parametrization.

Cutoff functions are widely used in potentials to limit their interaction distance. In MD simulations, this restricts the resulting nearest-neighbor list size, which in turn leads to much more computationally efficient calculations. The smoothness of the decay in the region of the potential's cutoff is very important for calculations involving surfaces and liquid environments since intense sampling of this region of the potential occurs under these circumstances. Additionally, smooth functions increase the stability of the numerical solution of the Lagrangian integrals at discrete time steps.<sup>41,42</sup> Each pair function in Eqs. (3), (4), and (6) utilizes a third-order polynomial spline to smoothly approach zero for interatomic spacings within the range  $r_1 < r < r_{\text{cut}}$ , where  $r_{\text{cut}}$  typically includes only the first nearest-neighbor shell.<sup>43</sup> The spline function  $S(r) = a + br + cr^2 + dr^3$  has parameters  $a$ ,  $b$ ,  $c$ , and  $d$  that can be determined for  $\beta_\sigma$ ,  $\beta_\pi$ , and  $\phi$  by equating

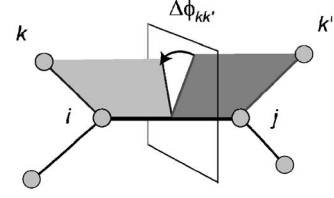


FIG. 2. Dihedral angle  $\Delta\phi_{kk'}$  for the four-body angle involving the  $k$ ,  $i$ ,  $j$ , and  $k'$  atoms around the  $ij$  bond.

the value and derivative of each function to the spline at  $r=r_1$  and by requiring that the spline function and its derivative be equal to zero at  $r=r_{\text{cut}}$ . Hence, the tails of the longer-range  $\beta_\sigma$ ,  $\beta_\pi$ , and  $\phi$  functions are smoothly replaced by the short-range spline function.

The  $\sigma$  bond order has been derived for systems with half-full valence shells and can be generalized to include systems with any valence band occupancy. A two-level BOP approximation for  $\sigma$  bonds with a half-full valence shell can be written

$$\Theta_{\sigma,ij}^{(1/2)} = 1 / \sqrt{1 + c_\sigma (\Phi_{ij,\sigma} + \Phi_{ji,\sigma})}, \quad (8)$$

where  $c_\sigma$  is an empirical parameter that compensates for some of the error introduced by a two-level  $\sigma$  bond-order approximation and the  $\Phi_{\sigma,ij}$  ( $\Phi_{\sigma,ji}$ ) term is given by

$$\Phi_{\sigma,ij} = \sum_{k,k' \neq i,j} g_{\sigma,jik}^2 \left( \frac{\beta_{\sigma,ik}}{\beta_{\sigma,ij}} \right)^2. \quad (9)$$

The  $g_\sigma$  function in Eq. (9) introduces angular-dependent contributions to bonding resulting from the overlap of the hybridized atomic orbitals. The three-body angular-dependent function between atoms  $i$ ,  $j$ , and  $k$  can be written

$$g_{\sigma,jik} = \frac{1 + p_\sigma (\cos \theta_{jik} - 1) + b_\sigma \cos 2\theta_{jik}}{1 + b_\sigma}, \quad (10)$$

where  $\theta_{jik}$  is the angle, centered at atom  $i$ , between vectors  $\vec{ij}$  and  $\vec{ik}$ . The three-body angular-dependent function has two free parameters ( $p_\sigma$  and  $b_\sigma$ ) that depend on the type of each of the  $i$ ,  $j$ , and  $k$  atoms in the angle. This allows incorporation of asymmetry in heteroatomic bonding environments.<sup>23,28</sup> Note that  $s$  orbitals have no angular dependence ( $p_\sigma=0$ ,  $b_\sigma=0$ ),  $p$  orbitals have a  $\cos \theta$  form ( $p_\sigma=1$  and  $b_\sigma=0$ ), and  $d_{z^2}$  orbitals have a  $\cos^2 \theta$  (or  $1 + \cos 2\theta$ ) dependence ( $p_\sigma=0$  and  $b_\sigma \neq 0$ ). The hybridized atomic orbitals overlap and form molecular orbitals with a combination of these basic angular dependences.<sup>30</sup> The  $b_\sigma$  parameter was introduced in an early form of the BOP (Ref. 31) and was implemented here to help in the parametrization of the potential for arsenic.

A general  $\sigma$  bond-order term that includes valence shell occupancy can be extrapolated from the half-full bond order by using a combination of symmetric and asymmetric bond-order functions<sup>29</sup>

$$\Theta_{\sigma,ij} = \Theta_{s,ij}(\Theta_{\sigma,ij}^{(1/2)}, f_{\sigma}) \left[ 1 - \left( f_{\sigma} - \frac{1}{2} \right) k_{\sigma} \frac{\mathcal{R}_{3\sigma,ij}}{1 + \frac{\Phi_{\sigma,ij} + \Phi_{\sigma,ji}}{2}} \right], \quad (11)$$

where  $\Theta_s(\Theta, f)$  is the symmetric band-filling function that modifies the half-full valence shell bond-order expression and the second term approximates the asymmetric eigenspectra with a skewing term that is proportional to the normalized three-member ring contribution. We employ a band-filling parameter  $f_{\sigma}$  and a skewing parameter  $k_{\sigma}$  in the symmetric and asymmetric terms. The  $f_{\sigma}$  parameter represents the number of electrons ( $e^-$ ) in the valence shell normalized by the full valence shell (eight electrons). Both  $f_{\sigma}$  and  $k_{\sigma}$  are dependent on the types of atoms  $i$  and  $j$ . The asymmetric three-member ring terms in Eq. (11) can be expressed in the form<sup>29</sup>

$$\mathcal{R}_{3\sigma,ij} = \sum_{k,k \neq i,j} g_{\sigma,jik} g_{\sigma,kji} g_{\sigma,ikj} \frac{\beta_{\sigma,ik} \beta_{\sigma,jk}}{\beta_{\sigma,ij} \beta_{\sigma,ij}}. \quad (12)$$

The symmetric band-filling function can be expressed as a series of splines that fit the functional to tight-binding calculations<sup>29</sup>

$$\Theta_s(\Theta_0, f) = \begin{cases} 2f, & 0 \leq f < f_0, \\ 2f_0 + 2\mathcal{F}(1 - 2f_0)[1 + \mathcal{F}(1 - c_s \mathcal{F})], & f_0 \leq f < 1 - f_0, \\ 2(1 - f), & 1 - f_0 \leq f \leq 1, \end{cases} \quad (13)$$

where

$$\mathcal{F} = \frac{f(1-f) - f_0(1-f_0)}{(1-2f_0)^2}, \quad (14)$$

$$c_s = \begin{cases} 0, & \Theta_0 > \frac{5}{8}, \\ 32\left(\frac{5}{8} - \Theta_0\right), & \Theta_0 \leq \frac{5}{8}, \end{cases} \quad (15)$$

$$f_0 = \frac{4}{3} \left( \Theta_0 - \frac{5}{8} \right). \quad (16)$$

An analytic expression for the  $\pi$  bond order was derived using the first two levels (sites) from the matrix form of the Lanczos algorithm.<sup>25,28</sup> The resulting two-site ( $\pi_+$  and  $\pi_-$ ) expression for a half-full valence shell with hops of lengths 2 and 4 is

$$\Theta_{\pi,ij} = \Theta_{\pi_+} + \Theta_{\pi_-}, \quad (17)$$

where

$$\Theta_{\pi_{\pm}} = 1 / \sqrt{1 + c_{\pi} \left( \frac{\Phi_{2\pi,ij} + \Phi_{2\pi,ji}}{2} \mp \sqrt{\Phi_{4\pi,ij}} \right)}. \quad (18)$$

The  $\Phi_{2\pi,ij}$  ( $\Phi_{2\pi,ji}$ ) terms are defined as

$$\Phi_{2\pi,ij} = \sum_{k,k \neq i,j} \left[ \hat{\beta}_{\pi,ik} \sin^2(\theta_{jik}) + 2 \left( \frac{\beta_{\pi,ik}}{\beta_{\pi,ij}} \right)^2 \right], \quad (19)$$

where

$$\hat{\beta}_{\pi,ik} = p_{\pi} \left( \frac{\beta_{\sigma,ik}}{\beta_{\pi,ij}} \right)^2 - \left( \frac{\beta_{\pi,ik}}{\beta_{\pi,ij}} \right)^2 \quad (20)$$

and  $p_{\pi}$  is the species-dependent parameter of the central atom  $i$ . The  $\Phi_{4\pi,ij}$  term contains four-body dihedral angles  $\Delta\phi_{kk'}$  that are important in  $\pi$  bonding,

$$\begin{aligned} \Phi_{4\pi,ij} = & \sum_{k,k \neq j} \sum_{k'=k+1,k' \neq j} \left[ \hat{\beta}_{\pi,ik}^2 \hat{\beta}_{\pi,ik'}^2 \sin^2 \theta_{jik} \sin^2 \theta_{jik'} \right. \\ & + \hat{\beta}_{\pi,ik}^2 \hat{\beta}_{\pi,jk'}^2 \sin^2 \theta_{jik} \sin^2 \theta_{ijk'} \\ & + \hat{\beta}_{\pi,ik'}^2 \hat{\beta}_{\pi,jk}^2 \sin^2 \theta_{ijk} \sin^2 \theta_{jik'} \\ & \left. + \hat{\beta}_{\pi,jk}^2 \hat{\beta}_{\pi,jk'}^2 \sin^2 \theta_{ijk} \sin^2 \theta_{ijk'} \right] \frac{\cos 2(\Delta\phi_{kk'})}{4}. \end{aligned} \quad (21)$$

Equation (22) sums from  $k$  to  $k'$  and therefore counts the neighbors of atoms  $i$  and  $j$  forming the  $ij$  bond. The dihedral angle  $\Delta\phi_{kk'}$ , defined in Fig. 2, is given by

$$\cos 2(\Delta\phi_{kk'}) = \frac{2[\cos \theta_{kik'} - \cos \theta_{jik'} \cos \theta_{jik}]^2}{\sin^2 \theta_{jik} \sin^2 \theta_{jik'}} - 1. \quad (22)$$

The addition of the dihedral angle in a  $\pi$ -bonding format is extremely important for modeling arsenic interactions with a dominant  $p^3$  valence shell.<sup>44,45</sup>

To summarize, we propose an analytic potential energy function [Eq. (1)] that is expressed in terms of bonding [Eq. (2)] and repulsive [Eq. (5)] energy components. The bonding energy has been split into  $\sigma$  and  $\pi$  bonding terms, each of which are the products of a bond integral and a bond order. The bond integrals [Eqs. (3) and (4)] and the repulsive energy [Eq. (6)] were approximated with two-body GSP functions. The  $\sigma$  bond order [Eq. (8)] with a half-full valence shell was used to interpolate the bond-order expression that incorporated explicit valence band filling [Eq. (11)]. This  $\sigma$  bond-order expression also contained a three-member ring term [Eq. (12)] that allowed implementation of an asymmetric density of states, which helps to either stabilize or destabilize close-packed structures. The  $\pi$  bond order [Eq. (17)] included hopping paths of length 4 [Eq. (22)] that facilitated incorporation of a dihedral angle.

## B. Parameters

There are 10 free material-specific parameters in the GSP functions for the repulsive and bond integral terms. The bond-order terms have 3 bond-dependent parameters and 4 additional angular parameters for the elemental system. Binary systems have a total of 8 angular parameters. Hence, the gallium and arsenic elemental systems have 17 parameters each, while the binary GaAs system has an additional 22

TABLE I. Bond-dependent BOP parameters for GaAs. The values depend on species types of atoms  $i$  and  $j$  that form a bond.

Symbol	Quantity	Ga-Ga	As-As	Ga-As
$r_0$	GSP reference radius (Å)	2.4235	2.1200	2.3800
$r_c$	GSP characteristic radius (Å)	2.4235	2.1200	2.3800
$m$	GSP attractive exponent	1.4509	1.3059	1.9652
$n$	GSP repulsive exponent	0.7255	0.6529	0.9826
$n_c$	GSP decay exponent	2.6234	2.6304	2.6234
$r_1$	Spline start radius (Å)	3.0000	3.0000	3.0000
$r_{\text{cut}}$	Spline cutoff radius (Å)	3.7000	3.6500	3.7000
$\phi_0$	Repulsive energy prefactor (eV)	1.5520	3.9800	2.1000
$\beta_{\sigma,0}$	$\sigma$ bond integral prefactor (eV)	1.5233	3.0877	1.7959
$\beta_{\pi,0}$	$\pi$ bond integral prefactor (eV)	0.0975	0.9263	0.3233
$c_\sigma$	Empirical $\Theta_\sigma$ parameter	1.5193	3.6016	0.8534
$c_\pi$	Empirical $\Theta_\pi$ parameter	1.0000	1.0000	1.0000
$f_\sigma$	Band filling fraction ( $e^-/8$ )	0.4456	0.6558	0.5000
$k_\sigma$	Skewing prefactor	-25.6485	0.7600	0.0000

parameters. There are thus a total of  $17+17+22$  (56) parameters to be determined. However, 17 parameters can be fixed prior to the fitting process. They included interatom bond lengths, such as  $r_0$ , which were equated and fixed to an estimate of the dimer separation distances. The cutoff parameters ( $r_c$ ) were also specified and therefore not included in the fitting process. The  $r_c$  parameters were initially fixed for the gallium, arsenic, and GaAs systems to include only the atoms of the first nearest-neighbor shell of the zb, NaCl, fcc, dc, and sc structures (3.70 Å). However, at the completion of the fitting process, the arsenic cutoff distance was shortened to 3.65 Å to include only the first 6 neighbors of the  $\alpha$ As phase. The  $r_1$  parameters were arbitrarily fixed at 3.00 Å. Additionally, the  $c_\pi$  parameters were set to unity as was originally derived for the  $\pi$  bond order.<sup>26,29</sup> The GaAs zb crystal structure has a half-full valence shell ( $f_\sigma=0.50$ ) and does not make use of the symmetric and asymmetric  $\sigma$  bond-order terms ( $k_\sigma=0$ ); therefore, these two additional parameters for the Ga-As bonds were not included in the fit.

The remaining  $12+12+15$  (39) unknown BOP parameters were determined using a method adapted from the work of Albe *et al.*,<sup>20</sup> which utilized a two-step parametrization approach for the GaAs material system described in detail in Appendix A. The material properties used to determine the 12 free BOP parameters for gallium were interatomic spacings, binding and cohesive energies, and bond stiffness data for the dimer and cubic structures. Similar data were used for fitting arsenic parameters. However, the structural and cohesive energy of the  $\alpha$ As phase and the cohesive energy of the arsenolamprite phase were also included in the fitting process. The 15 binary GaAs parameters were determined from dimer, trimer, and cubic crystal properties. Additionally, the sc16 (space group  $Pa\bar{3}$ ) cohesive energy, zb elastic constants, and unrelaxed vacancy and antisite defect formation energy values were restricted within a defined range during the fitting process. A good fit for the GSP parameters ( $m$ ,  $n$ ,  $n_c$ , and  $\phi_0$ ) was obtained and is summarized among the other bond-dependent BOP parameters ( $\beta_{\sigma,0}$ ,  $\beta_{\pi,0}$ ,  $c_\sigma$ ,  $c_\pi$ ,  $f_\sigma$ , and

$k_\sigma$ ) in Table I. In addition to these two-body parameters, the three-body angular parameters ( $p_\pi$ ,  $p_\sigma$ , and  $b_\sigma$ ) are summarized in Table II.

### III. EVALUATION OF THE POTENTIAL

The GaAs parametrization of the BOP was assessed by examining predicted properties relevant to the atomic assembly of epitaxial thin films grown from the vapor phase.<sup>23</sup> These include the bulk atomic volume, cohesive energy, and the elastic constants for various gallium, arsenic, and GaAs structures; the zb GaAs melting temperature; the arsenic and gallium dimer, trimer, and tetramer binding energies and structures; various GaAs defect formation energies; and the surface free energies of GaAs (001) surface reconstructions. An analytic implementation of the interatomic energy and forces in a Lagrangian MD code<sup>46,47</sup> and in a symbolic computing environment<sup>48</sup> were used to analyze the parametrized BOP.

#### A. Small-cluster properties

During vapor deposition, molecular arsenic (dimers and tetramers) and gallium atoms assemble to form GaAs. This

TABLE II. BOP angular parameters for GaAs. These parameters are dependent on the three atoms that define the angle  $\theta_{jik}$ , where atom  $i$  is the central atom. It is assumed that the parameters for  $jik$  and  $kij$  are equal.

$jik$	$p_\pi$	$p_\sigma$	$b_\sigma$
Ga-Ga-Ga	0.7202	0.7947	0.1036
As-As-As	0.4271	0.8785	0.1458
As-Ga-As	—	0.6947	0.0391
Ga-As-Ga	—	0.7658	0.0000
Ga-Ga-As	—	0.8120	0.1275
As-As-Ga	—	0.8729	0.1642

TABLE III. Gallium cluster interatomic spacing ( $r$  in Å), primary bond angles ( $\theta$  in degrees), and binding energy ( $E_B$  in eV/atom) as predicted by DFT and BOP calculations. Dashes (-) signify that data are either not defined or are unavailable.

Structure	DFT <sup>a</sup>			BOP		
	$E_B$	$r$	$\theta$	$E_B$	$r$	$\theta$
Dimer	0.91	2.416	-	0.78	2.423	-
Trimer	1.03	2.661	60.0	1.17	2.551	60.0
Square	1.26	2.720	90.0	1.31	2.399	90.0
Rhombus	-	-	-	1.43	2.472	76.0
Tetrahedron	-	-	-	1.34	2.666	60.0
Four atom chain	-	-	-	0.93	2.524	-

<sup>a</sup>Reference 22.

assembly process is sensitive to the structure and bond strength of these incident molecules<sup>49</sup>; therefore, reasonable predictions of bond energetics and structures with regard to small clusters are needed to accurately model these processes. Additionally, cluster properties are useful for evaluating the BOP by testing radial and angular bond-dependent structural parameters. To this end, the structure and binding energies (free atom energy minus the energy of the bound cluster) of elemental and binary clusters (dimers, trimers, and tetramers) were evaluated using the BOP. The dimer bond stiffness was measured by the ground-state wave numbers  $\omega = \sqrt{d^2E/dr^2/\mu}/(2\pi c)$ , where  $\mu$  is the reduced mass,  $c$  is the speed of light in a vacuum, and  $d^2E/dr^2$  is the curvature of the dimer energy function and was also compared to experimental values.

The structure and binding energy per atom ( $E_B$ ) of small gallium clusters are summarized in Table III. These have not been determined experimentally; therefore, *ab initio* calculations were used for comparison with the BOP predictions. Inspection of Table III indicates that the dimer binding energy predicted by the BOP was roughly 15% smaller than a generalized gradient approximation (GGA) density functional theory (DFT) prediction,<sup>22</sup> but the separation distances were almost exactly the same. The dimer wave number was predicted to be 168.8 cm<sup>-1</sup> compared to an experimentally

measured value of 165 cm<sup>-1</sup>.<sup>50</sup> For the equilateral triangle trimer structure, the predicted BOP binding energy and interatomic spacing matched the GGA DFT calculations reasonably well (within 14% and 4%, respectively). However, the GGA DFT calculations predict a square structure as the lowest-energy tetramer structure, while the BOP calculations predict the rhombus structure to be 0.12 eV/atom more stable than the square.

The arsenic dimer, trimer, and tetramer data are summarized in Table IV. The arsenic dimer spacing and binding energy for GGA DFT, experimental, and BOP data were all within a few percent of each other.<sup>22,50</sup> The arsenic dimer wave number predicted by the BOP was 268.7 cm<sup>-1</sup>, which is 37.5% below the value (429.6 cm<sup>-1</sup>) experimentally observed.<sup>51</sup> The GGA DFT and BOP predictions both indicate that an isosceles triangle is the most stable trimer structure. The BOP arsenic trimer binding energy, bond lengths, and bond angle were all reasonably close to both the experimental<sup>50,52</sup> and GGA DFT<sup>22</sup> data. Experimental studies indicate that the tetrahedron structure is the lowest-energy tetramer structure,<sup>53</sup> and this is confirmed by GGA DFT calculations.<sup>22</sup> However, the BOP predicts a rhombus structure to be 0.59 eV/atom more stable than the tetrahedron structure.

BOP predictions for the GaAs dimers, trimers, and stoichiometric tetramer structures are compared to GGA DFT

TABLE IV. Arsenic cluster interatomic spacing ( $r$  in Å), primary bond angles ( $\theta$  in degrees), and binding energy ( $E_B$  in eV/atom) as reported by experimental measurements and predicted by GGA DFT and the BOP calculations. Dashes (-) signify that data are either not defined or are unavailable.

Structure	Experiment <sup>a</sup>			GGA DFT <sup>b</sup>			BOP		
	$E_B$	$r$	$\theta$	$E_B$	$r$	$\theta$	$E_B$	$r$	$\theta$
Dimer	1.98	2.103	-	2.03	2.122	-	1.99	2.120	-
Trimer	2.14	-	-	2.13	2.332 <sup>c</sup>	65.0	1.82	2.339 <sup>c</sup>	72.9
Tetrahedron	2.55	2.435	60.0	2.68	2.460	60.0	1.63	2.637	60.0
Rhombus	-	-	-	-	-	-	2.22	2.381	78.9
Rectangle	-	-	-	-	-	-	2.21	2.111/3.000	90.0
Four atom chain	-	-	-	-	-	-	1.72	2.354	-

<sup>a</sup>References 50, 52, and 53.

<sup>b</sup>Reference 22.

<sup>c</sup>Isosceles triangle side length.

TABLE V. GaAs cluster interatomic spacing ( $r$  in Å), primary bond angles ( $\theta$  in degrees), and binding energy ( $E_B$  in eV/atom) as predicted by GGA DFT and BOP calculations. Dashes (-) signify that data are either not defined or are unavailable. Experimental data for the dimer was  $E_B=1.03$  eV/atom and  $r=2.53$  Å Ref. 54.

Structure	GGA DFT <sup>a</sup>			BOP		
	$E_B$	$r$	$\theta$	$E_B$	$r$	$\theta$
Dimer	1.02	2.670	-	1.42	2.277	-
Ga-As-Ga <sup>b</sup>	1.48	2.453	101.09	1.42	2.375	109.78
As-Ga-As <sup>b</sup>	1.89	2.859	45.45	1.71	2.549	63.27
Rhombus	2.04	2.776	49.10	1.80	2.448	88.5
Quadrilateral <sup>d</sup>	-	-	-	1.92	2.225 (As-As) 2.512 (Ga-Ga) 2.473 (Ga-As)	86.7–93.3

<sup>a</sup>Reference 22.

<sup>b</sup>Isosceles triangle: side length and apex angle are given.

<sup>c</sup>Stoichiometric rhombus with Ga-As-Ga-As structure; the bond lengths for As-As are less than that for Ga-Ga.

<sup>d</sup>Stoichiometric rectangle like tetramer with Ga-Ga-As-As structure.

data in Table V. The GaAs dimer binding energy predicted by the BOP was 40% greater and the separation distance 10%–15% less than the experimental and GGA DFT data.<sup>22,54</sup> The GaAs dimer wave number predicted by the BOP (297.8 cm<sup>-1</sup>) was 38.5% higher than the experimentally measured value (215 cm<sup>-1</sup>).<sup>54</sup> These discrepancies for the GaAs dimer represent a limitation of the BOP, where the  $\sigma$  and  $\pi$  bond-order values saturate at  $\Theta_\sigma=1$  and  $\Theta_\pi=2$  for the GaAs dimer. However, this is not the case for most bulk structures, which generally yield bond-order values below these maximums. Therefore, the attractive bond energy ( $U_{\text{bond}}$ ) makes its strongest contribution for dimers, which reduces the dimer interatomic spacing below that of the GaAs zb phase. As a result, the experimental GaAs dimer spacing cannot be predicted if the integrity of the zb phase is to be preserved.

The arsenic-centered trimer (Ga-As-Ga) was well predicted by the BOP with binding energies and structures all within 8.5% of GGA DFT data.<sup>22</sup> The gallium-centered trimer (As-Ga-As) had a 40% larger bond angle than the GGA DFT data, but the bonding energy and bond lengths were less than 11% different. The most stable stoichiometric tetramer predicted by GGA DFT was the Ga-As-Ga-As rhombus, while the lowest-energy BOP-predicted structure was a distorted Ga-Ga-As-As squarelike quadrilateral structure.

The low-energy tetramer structures all deviated from the available GGA DFT and experimental data. We found that our parametrization was not sufficiently transferable to predict both bulk and tetramer structures within a single parameter set. It is possible that the incorporation of additional physics is necessary to allow both environments to be modeled. For example, the inclusion of additional hopping paths into the bond-order terms might address this issue. Additionally, the two-center approximation, as implemented with the two-body GSP functions, may also limit transferability between bulk and cluster properties.<sup>55</sup>

Despite these limitations, the BOP-predicted binding energies of the lowest-energy structures were generally in good

agreement with GGA DFT data. The strong molecular arsenic bonding in clusters, which is very important for modeling vapor deposition, was also well predicted. Similarly, good predictions were made for the weak gallium binding and moderate GaAs binding trends. The GaAs BOP is therefore anticipated to perform reasonably well for the modeling of the molecular species involved in GaAs vapor deposition.

## B. Bulk lattice structures

The sensitivity of the potentials to the local bonding environment can also be investigated by comparisons with the structure, volume ( $V$ ), cohesive energy ( $\Delta E$ ), and elastic constants (usually the bulk modulus  $B$ ) of gallium, arsenic, and GaAs crystalline phases with atomic coordinations between 4 and 12. The cohesive energy is a negative quantity that measures the difference in the total energy of atoms in their bulk bound state compared to the energy of the atoms in their free unbonded state. The experimental enthalpies are generally reported at 298 K, as compared to DFT and BOP energies, which are usually calculated at 0 K. The direct comparison between these values (both reported with respect to the free atom energy state) at constant pressure ( $P$ ) was previously justified based on the small difference in enthalpy values between 298 K and 0 K for gallium (>1%), arsenic (~6%), and GaAs (>1%).<sup>23</sup> Therefore, cohesive energy values deduced at 298 K for gallium and GaAs and at both 0 K and 298 K for arsenic were included in the analysis,<sup>18,56</sup> because  $\Delta H = \Delta E + \Delta(PV) \approx \Delta E$ .

The properties of a large number of crystalline phases were also evaluated and are identified using either the crystalline prototype or common name; see Appendix B for additional crystallographic information. The abbreviations used are zb (zinc blende), sc16 (simple cubic with 16 atoms in the unit cell), fcc (face-centered cubic), bcc (body-centered cubic), sc (simple cubic), and dc (diamond cubic).

Experimental values for atomic volumes, enthalpies, and bulk moduli at 298 K and atmospheric pressure for the stable

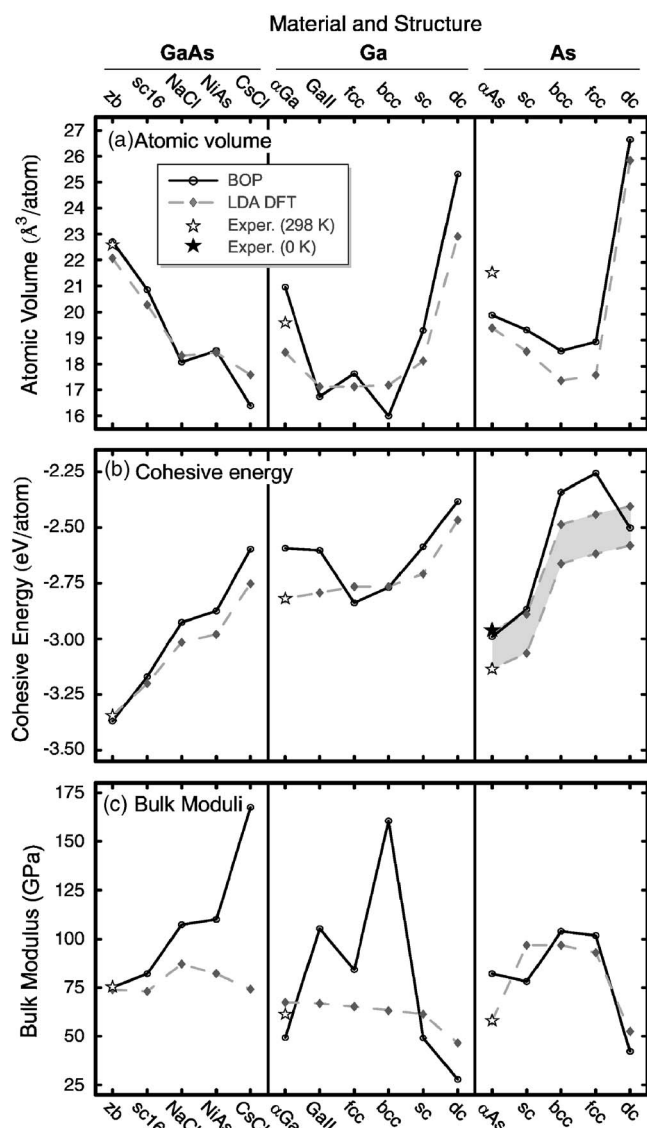


FIG. 3. The BOP, LDA DFT, and experimental data of (a) atomic volume ( $\text{\AA}^3/\text{atom}$ ), (b) cohesive energy (eV/atom), and (c) bulk modulus (GPa) for selected GaAs, gallium, and arsenic phases. Experimental enthalpies at 298 K are used as the absolute energy point for the relative LDA DFT energy data. For the  $\alpha\text{As}$  phase, a 6% change in enthalpy between 298 K and 0 K is noted by the shaded region.

zb,<sup>18,57–59</sup>  $\alpha\text{Ga}$ ,<sup>18,57,60,61</sup> and  $\alpha\text{As}$ <sup>18,57,60,62</sup> phases were compiled and are summarized in Fig. 3. The material properties for a wide range of structures have been calculated using the local density approximation (LDA) DFT at 0 K for elements<sup>20</sup> and the binary GaAs system<sup>19</sup> and are also shown in Fig. 3. The reported elemental gallium data<sup>20</sup> was augmented by the LDA (ultrasoft pseudopotential<sup>63</sup>) calculation of the gallium bcc phase data with the Vienna *ab initio* simulation program (VASP).<sup>64–67</sup> LDA DFT data cohesive energies are generally only given relative to the lowest-energy phases<sup>19,20</sup>; therefore, the data were shifted to experimental energies so that an estimate of absolute energies could be used to evaluate the BOP predictions.

Examination of Fig. 3(a) indicates that the BOP-predicted atomic volumes per atom were generally within 8% of the LDA DFT atomic volume predictions. The atomic volumes of the Ga- $\alpha\text{Ga}$  and Ga-dc crystal structures were the only structures with deviations outside this range. The relative orders of the BOP and LDA DFT atomic volume values were identical except for the Ga-bcc structure, which has a smaller atomic volume relative to the fcc and Ga-II (of the  $I\bar{4}3d$  space group) structures rather than a larger value as predicted by LDA DFT.<sup>20</sup>

In the BOP, the free atom state was defined to have zero energy; therefore, the potential energy in Eq. (1) can be used to directly calculate cohesive energies. The cohesive energies per atom are summarized in Fig. 3(b). These energies were all within 8% of the LDA DFT and experimental data. The low-energy gallium structure was approximated by the choice of an fcc solid (see Appendix A for an explanation), which disrupted the relative energy ordering. The experimentally observed low-energy  $\alpha\text{Ga}$  and metastable Ga-II phases were predicted by the GaAs BOP to be around 0.2 eV/atom less stable than experimental data and LDA DFT predictions. In addition to these gallium phases, the As-dc structure also had a lower relative energy than the As-fcc and As-bcc phases, when compared with the LDA DFT data. Despite these discrepancies with LDA DFT predictions, the general trend of the energies were well reproduced by this parametrization of the BOP.

Bulk moduli data from LDA DFT calculations and experimental measurements are compared to the BOP predictions in Fig. 3(c). The bulk moduli were approximated by the BOP analytic calculations without internal relaxation for the selected structures. For cubic structures, this approximation is negligible; however, it can become more significant for the non-cubic phases. The comparison between LDA DFT (also unrelaxed) and the BOP predictions were within 42% of each other, except for gallium in bcc-like configurations. These CsCl, bcc, and Ga-II phases significantly overpredicted the bulk moduli data predicted by LDA DFT. The deviation from LDA DFT predictions, though significant, is similar or less than the discrepancies found using other interatomic potentials.<sup>23</sup>

When calculating the bulk moduli with the BOP, the environmentally dependent bond orders are virtually constant as volume is varied. Therefore, the reduced accuracy of the elastic response is largely dependent on the two-body function of Eq. (7). The two-body function simply calculates a repulsive or bond integral value based on the distance between the two atoms and does not consider the effect neighboring atoms may have on screening the interaction. The inclusion of the screening may positively affect the energy versus volume properties.

In addition to bulk moduli data, the three independent elastic constants for the GaAs zb structure are shown in Table VI. The unrelaxed elastic constants are denoted by the superscript (0) and reported for comparison with the values in DFT calculations. The  $c_{44}$  elastic constant shows a significant change when atoms are allowed to relax during calculations; however, this is not the case for the  $c_{11}$  and  $c_{12}$  elastic constants, which exhibit little relaxation. The elastic



TABLE VI. GaAs zb single-crystal elastic constants as predicted by the BOP and DFT calculations and observed in experiments. Calculations of  $c_{44}$  that do not allow internal relaxation are labeled  $c_{44}^{(0)}$ . All data have units of GPa.

$c_{ij}$	Expt. (298 K) <sup>a</sup>	LDA DFT <sup>b</sup>	BOP
$c_{11}$	118.1	123.0	117.4
$c_{12}$	53.2	58.0	53.5
$c_{44}$	59.2	62.0	49.9
$c_{44}^{(0)}$	-	75.0	73.6

<sup>a</sup>Reference 59.

<sup>b</sup>Reference 68.

constants predicted by this parametrization of BOP match experimental observations at 298 K<sup>59</sup> and LDA DFT calculations<sup>68</sup> to within 5% for all but the relaxed elastic constant data  $c_{44}$ . The relaxed  $c_{44}$  elastic constant predicted by the GaAs BOP was 9.3 GPa less stiff than the experimental measurement and 12.1 GPa less stiff than the LDA DFT predictions. The Cauchy pressure ( $c_{12}-c_{44}$ ) for experimental [-6 GPa (Ref. 59)] and DFT [-4 GPa (Ref. 68)] data are negative. However, using the relaxed values predicted by the BOP, a positive Cauchy pressure of 3.69 GPa was calculated.

The origin of positive Cauchy pressure predicted by the BOP is the repulsive electrostatic part of the total energy.<sup>69</sup> For cubic systems, a positive Cauchy relation can be traced to the stress component  $\sigma_{11}$ , which is strongly positive for the bonding part [Eq. (2)] of a BOP. To balance this contribution from the bonding energy, a negative curvature from the repulsive energy is needed to produce a negative Cauchy relation, which is not provided by the two-body repulsive term [Eq. (5)]. The implementation of the repulsive screening of valence orbitals<sup>70</sup> and an explicit repulsive promotion energy term should recover an experimentally valid Cauchy relation.<sup>28</sup>

TABLE VII. Point defect formation energies and structures predicted by GaAs BOP and DFT calculations. Defect formation energies ( $\Omega_{\Delta\mu=0}=E'_D$ ), normalized interatomic separation distances ( $\hat{r}_{NN}$ ), and number (No.) and type of surrounding atoms are identified for vacancy ( $V_{\text{Ga}}$  and  $V_{\text{As}}$ ), antisite ( $\text{Ga}_{\text{As}}$  and  $\text{As}_{\text{Ga}}$ ), and interstitial ( $\text{Ga}_i$  and  $\text{As}_i$ ) point defects in zb GaAs. When more than one type of atom surrounds the defect, the positions and types are separated by slashes (/). Dashes (-) indicate that DFT data are unavailable.

Defect	DFT <sup>a</sup>			BOP		
	$E'_D$	$\hat{r}_{NN}$	Type(No.)	$E'_D$	$\hat{r}_{NN}$	Type(No.)
$V_{\text{Ga}}$	3.15	0.88	As(4)	3.28	0.99	As(4)
$V_{\text{As}}$	3.10	0.89	Ga(4)	2.93	1.03	Ga(4)
$\text{Ga}_{\text{As}}$	2.12	0.99±0.06	Ga(4)	2.03	1.06	Ga(4)
$\text{As}_{\text{Ga}}$	2.48	1.06	As(4)	2.50	1.05	As(4)
$\text{Ga}_i$ (tetrahedral)	2.98	1.06	As(4)	2.66	1.03	Ga(4)
				4.14	1.08	As(4)
$\text{As}_i$ (tetrahedral)	5.04	-	Ga(4)	4.47	1.07	Ga(4)
				3.32	1.03	As(4)
$\text{Ga}_i$ ( $\langle 110 \rangle$ dumbbell)	3.53	-	Ga(1)/As(3)	4.97	1.01/1.01–1.02	Ga(1)/As(3)
$\text{As}_i$ ( $\langle 110 \rangle$ dumbbell)	4.07	1.01/1.07	As(1)/Ga(3)	3.82	0.94/1.02–1.08	As(1)/Ga(3)
$\text{Ga}_i$ ( $\langle 100 \rangle$ dumbbell)	-	-	-	3.86	0.89/0.96	Ga(1)/As(2)
$\text{As}_i$ ( $\langle 100 \rangle$ dumbbell)	-	-	-	4.68	0.88/0.99	As(1)/Ga(2)

<sup>a</sup>References 74 and 80.

The BOP-predicted atomic volume, cohesive energy, and elastic constants for GaAs are in generally good agreement with independent assessments and indicate that it can perform well over a wide range of environments. This suggests it is acceptable for vapor deposition applications.

### C. Melting temperature

At the melting temperature, the potential energy close to the cutoff distance is dynamically sampled. The prediction of a melting temperature therefore serves as an additional useful test of a potential. The GaAs melting temperature for the BOP was estimated using a method developed by Morris *et al.*,<sup>71</sup> in which a half-liquid, half-crystalline MD supercell was allowed to reach an equilibrium temperature under constant pressure. Here, a supercell consisting of 6400 atoms (100 planes with 64 atoms in each plane) was used to calculate the solid-liquid phase transition temperature. The supercell was initially divided into two temperature-controlled regions—one well above the melting temperature and the other well below. After 20 ps, one side had melted while the other remained crystalline. The temperature control was then removed and the system thermally equilibrated. After 500 ps of MD simulation, the boundary between the liquid and solid phases had ceased to move. The temperature of this (equilibrium) state was then taken as the melting temperature. The melting temperature predicted by GaAs BOP was  $1950 \pm 50$  K, which is reasonably close to the experimentally determined melting temperature of 1513 K at atmospheric pressure.<sup>72</sup> The BOP value overestimates this temperature by 28%. Previous studies have linked discrepancies in the melting behavior to the cutoff distance approximation,<sup>73</sup> which may be the case here.

### D. Point defects

In the GaAs zb lattice, the point defects encountered include gallium and arsenic vacancies ( $V_{\text{Ga}}$  and  $V_{\text{As}}$ ), gallium

antisites ( $\text{Ga}_{\text{As}}$ ) in which gallium sits on an arsenic site in the GaAs lattice, arsenic antisites ( $\text{As}_{\text{Ga}}$ ), and a variety of gallium and arsenic interstitials ( $\text{Ga}_i$  and  $\text{As}_i$ ).<sup>74,75</sup> Their concentrations depend on the defect formation energy growth, temperature, flux composition, and deposition rate.<sup>75,76</sup> The relative populations of the point defects can be estimated from their defect formation energies  $\Omega$ .<sup>77</sup> Utilizing the method proposed by Zhang and Northrup,<sup>77,78</sup> the energy of a neutral point defect can be expressed as

$$\Omega(\Delta\mu) = E'_D - \frac{1}{2}(n_{\text{Ga}} - n_{\text{As}})\Delta\mu, \quad (23)$$

where  $n_{\text{Ga}}$  and  $n_{\text{As}}$  are the number of gallium and arsenic atoms in a computational cell.

The defect formation energies are linearly dependent on the environmental conditions, which are addressed by the change in chemical potential,<sup>77-79</sup>

$$\Delta\mu = (\mu_{\text{Ga}} - \mu_{\text{As}}) - (\mu_{\text{Ga}}^{(\text{bulk})} - \mu_{\text{As}}^{(\text{bulk})}), \quad (24)$$

where  $\mu_{\text{Ga}}$  and  $\mu_{\text{As}}$  are the environment-dependent gallium and arsenic chemical potentials and  $\mu_{\text{Ga}}^{(\text{bulk})}$  and  $\mu_{\text{As}}^{(\text{bulk})}$  are the chemical potentials of the low-energy arsenic and gallium bulk phases. At 0 K, the bulk chemical potential values are equivalent to the cohesive energies per formula unit (f.u.) of the bulk systems. The  $\Delta\mu$  values are constrained between  $\pm\Delta H$ ,<sup>77</sup> where  $\Delta H$  is the formation enthalpy for GaAs per f.u. The predicted heat of formation at 0 K from the GaAs BOP is  $\Delta H_f = -0.91$  eV/f.u. and was calculated from the cohesive energy data in Appendix B. The experimental value is  $\Delta H_f = -0.74$  eV/f.u. at 298 K,<sup>18</sup> and is estimated at 0 K to be around  $-0.89$  eV/f.u.<sup>23,56</sup>

The neutral defect formation energy term, which is independent of environmental conditions ( $E'_D$ ), is defined as<sup>77,78</sup>

$$E'_D = E_D - \frac{1}{2}(n_{\text{Ga}} - n_{\text{As}})\mu_{\text{GaAs}}^{(\text{bulk})} - \frac{1}{2}(n_{\text{Ga}} - n_{\text{As}})(\mu_{\text{Ga}}^{(\text{bulk})} - \mu_{\text{As}}^{(\text{bulk})}), \quad (25)$$

where  $E_D$  is the total energy of a supercell that contains the defect. The  $E'_D$  values were calculated for gallium and arsenic vacancies ( $V_{\text{Ga}}$  and  $V_{\text{As}}$ ), gallium and arsenic antisites ( $\text{Ga}_{\text{As}}$  and  $\text{As}_{\text{Ga}}$ ), and three types of gallium and arsenic self-interstitial ( $\text{Ga}_i$  and  $\text{As}_i$ ) point defects. The interstitial point defects considered include the tetrahedral,  $\langle 110 \rangle$  dumbbell, and  $\langle 100 \rangle$  dumbbell types.<sup>80</sup> The dumbbell interstitials can be imagined to be formed by splitting an on-site arsenic or gallium atom into two atoms and separating them with their bond aligned along either the  $\langle 100 \rangle$  or  $\langle 110 \rangle$  direction.<sup>80,81</sup> The periodic computational cell used to calculate defect formation energies with *ab initio* LDA DFT methods had 64 atoms,<sup>74,80</sup> while the BOP data were calculated using a 512-atom cell. The low-energy defect structures were minimized at 0 K using a conjugate gradient method.<sup>82</sup>

The local structure around each defect was also evaluated. The interatomic bond lengths ( $r$ ) that connect a given defect to the surrounding atoms in the crystal were measured and normalized by a Ga-As reference bond length for the perfect

GaAs zb crystal ( $r_0$ ). The resulting normalized bond length  $\hat{r}_{NN} = r/r_0$  characterizes bond length expansion and contraction compared to the perfect crystal.

The  $E'_D$  and  $\hat{r}_{NN}$  values from LDA DFT<sup>74,80</sup> and BOP calculations are summarized in Table VII. The vacancy and antisite formation energies calculated by the BOP were  $<5.5\%$  of the LDA DFT reference data.<sup>74</sup> This can be contrasted with the evaluations<sup>23,74</sup> of previous GaAs parametrizations of the Tersoff<sup>83</sup> and Stillinger-Weber<sup>84</sup> potentials, which deviated from the reference formation energy data by an average of 17%–133%. The normalized nearest-neighbor bond lengths ( $\hat{r}_{NN}$ ) were near unity and had little inward or outward relaxation for the BOP vacancies. The LDA DFT calculations predicted significant inward relaxation around the vacancies. The local relaxation predicted by LDA DFT was also not well modeled by three of the four Tersoff potentials previously evaluated.<sup>74</sup> The local bonding environment predicted by LDA DFT around the antisites was reasonably captured by the BOP and all the previous parametrizations.

The lowest-energy interstitials for the BOP were those on tetrahedral sites. This was a good approximation for the gallium interstitial; however, it was not consistent with DFT predictions for the arsenic interstitial. In fact, the  $\text{As}_i$  (tetrahedral) was 0.5 eV more stable than the DFT-predicted  $\langle 110 \rangle$  dumbbell arsenic interstitial.<sup>74</sup> The formation energies for the lowest-energy interstitial defects showed that the BOP underpredicted the LDA DFT data by 10.7% ( $\text{Ga}_i$ ) and 18.4% ( $\text{As}_i$ ). The underpredicted formation energies for both gallium and arsenic interstitials indicate that the defect concentrations are likely to be slightly elevated during thin film growth. Nevertheless, this represents a significant improvement over an average of 77%–99% for interstitial formation energies predicted by previous parametrized potentials.<sup>23,74</sup> The local environments around each interstitial in the BOP (and previous potentials) were generally not well predicted for the arsenic interstitials. Only the parametrization by Sayed *et al.*<sup>85</sup> predicted reasonably close formation energies and local environments; however, this potential was much less accurate with regard to antisite and vacancy formation energies.<sup>74</sup>

The formation energy predictions of the BOP calculations are acceptably well represented by this potential and are considerably better than those of previously parametrized potentials. However, the issues with local bonding environments around vacancies and interstitials were approximated. These effects may ultimately be addressed by accounting better for local changes in electronic structure<sup>86</sup> with either screening functions<sup>55</sup> or explicit charge transfer terms.<sup>16</sup> Even so, the relative formation energy order is quite similar to the DFT results. MD simulations of vapor deposition under arsenic-rich conditions and relatively high temperatures will therefore predict that arsenic antisite defects are the most prevalent, which is consistent with experimental observations.<sup>75</sup>

### E. GaAs surfaces

The GaAs (001) surface can exhibit many reconstructed structures.<sup>87-90</sup> These include the experimentally validated arsenic-terminated  $\beta 2(2 \times 4)$ ,<sup>91-93</sup> arsenic-terminated  $\alpha 2(2$

$\times 4$ ),<sup>94</sup> arsenic-rich  $c(4 \times 4)$ ,<sup>95,96</sup> and gallium-rich  $\zeta(4 \times 2)$ <sup>97</sup> surface reconstructions. The surface temperature, composition of the vapor above the surface, and the deposition rate during film growth all combine to determine the reconstruction structure that forms on a surface.<sup>98</sup>

A surface free energy diagram can be used to represent the surface reconstructions that form under equilibrium conditions as the vapor composition is varied. The surface free energy per unit area,  $\gamma$ , can be calculated by assuming that the arsenic and gallium atoms in the vapor freely exchange between the bulk material (the thermodynamic reservoir) and an atmospheric vapor (atom reservoir)<sup>79,99</sup> in a similar manner to that discussed in the previous section. The gallium and arsenic atoms in these reservoirs have chemical potentials  $\mu_{\text{Ga}}$  and  $\mu_{\text{As}}$ , respectively, which under equilibrium conditions are related.<sup>79</sup> This allows the influence of the vapor composition to be represented by a single chemical potential difference ( $\mu_{\text{As}} - \mu_{\text{As}}^{(\text{bulk})}$ ), where  $\mu_{\text{As}}^{(\text{bulk})}$  is the chemical potential of the low-energy bulk arsenic crystal at 0 K (i.e., cohesive energy). The relative arsenic chemical potential is limited between 0 (arsenic-rich) and  $\Delta H_f$  (gallium-rich) conditions,<sup>79,99</sup> where the BOP predicts  $\Delta H_f = -0.91$  eV/f.u. (at 0 K) and experimental data indicate  $\Delta H_f = -0.74$  eV/f.u. (at 298 K)<sup>18</sup> and  $\Delta H_f = -0.89$  eV/f.u. (at 0 K).<sup>23,56</sup> The surface free energy per unit area can then be calculated as a function of this chemical potential difference for any atom configuration and composition by following standard methods detailed elsewhere.<sup>79,99,100</sup> Results have been obtained from DFT<sup>79,97,99</sup> and interatomic potentials.<sup>23,100,101</sup>

The surface free energy diagram predicted by the BOP was obtained using a computational supercell with 1500–1700 atoms (25–27 layers with 64 atoms/layer measuring  $32 \text{ \AA} \times 32 \text{ \AA}$ ) for each reconstructed surface.<sup>99,100,102</sup> The cell had periodic boundary conditions in the lateral directions and identical free surfaces on the top and bottom. The central plane was fixed and the entire system was then relaxed using the conjugate gradient method.<sup>82</sup>

The BOP-predicted, low-energy (001) surface reconstructions have simple dimer-row structures corresponding to an arsenic-terminated  $(2 \times 1)$  reconstruction for arsenic-rich conditions and a gallium-terminated  $(1 \times 2)$  reconstruction for gallium-rich conditions, Fig. 4. This result is generally consistent with previous predictions with interatomic potentials.<sup>23</sup> The simplified surface structures do not capture the additional trench features of the  $\beta 2(2 \times 4)$  surface reconstruction that stabilizes under high temperatures.<sup>87</sup> Nevertheless, the dimer-row surfaces represent a reasonable approximation when formation of complex surface reconstructions is hindered by the reduced atom mobility, as is the case during low-temperature molecular beam epitaxial growth.<sup>103</sup>

Because of the coarse graining of the electron degree of freedom, the occupancy of dangling surface bonds and general conservation of electrons are not explicitly treated in the BOP or other empirical potentials. The electron redistribution on surfaces has been shown to play a significant role in stabilizing (001) GaAs surface reconstructions.<sup>5,104,105</sup> To address this redistribution of electrons on the surface, additional physics must be added to the potentials to destabilize the  $(1 \times 2)$  and  $(2 \times 1)$  surface reconstructions. Using the

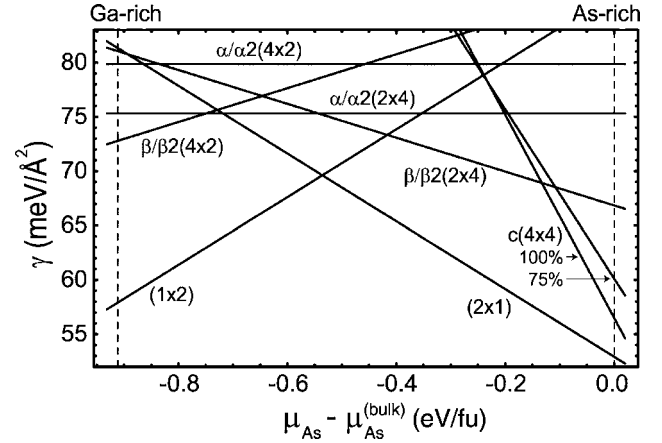


FIG. 4. GaAs (001) surface free energies for select surface reconstructions as predicted by the BOP. The  $\alpha(2 \times 4)$  and  $\alpha 2(2 \times 4)$  surface reconstructions have almost identical surface free energies and are shown as a single line and are labeled as  $\alpha/\alpha 2(2 \times 4)$ . The same notation was applied for the  $\alpha/\alpha 2(4 \times 2)$ ,  $\beta/\beta 2(2 \times 4)$ , and  $\beta/\beta 2(4 \times 2)$  surface reconstructions. The 100% and 75% coverages of the  $c(4 \times 4)$  surfaces are both shown.

well-known electron counting (EC) rule,<sup>5,105</sup> a simple energy penalty was recently proposed for static systems by calculating the square of the difference between the total number of electrons in the system and the total number of available low energy sites (i.e., covalent bonds and arsenic dangling bonds).<sup>100</sup> This EC energy term ( $U_{\text{EC}}$ ) can be added to Eq. (1) for the treatment of surfaces:

$$E = U_{\text{bond}} + U_{\text{rep}} + U_{\text{EC}}. \quad (26)$$

When applied to the GaAs surface, the  $U_{\text{EC}}$  term is minimized when the surface covalent and arsenic dangling bonds are fully occupied (2 electrons) and the gallium dangling bonds are empty (0 electrons).<sup>5,105</sup> Surface structures that have more or less electrons than the number required to exactly match these occupancies are then considered unstable and incur a positive EC energy penalty ( $U_{\text{EC}}$ ).<sup>87</sup>

This global EC approach has been generalized for MD by making a continuous and differentiable set of equations that link the system's EC energy to the local atom positions.<sup>106</sup> This local EC potential utilized the empirically determined EC rules for the distribution of electrons between covalent and dangling bonds to dynamically solve the electron occupation around each atom. By design, the EC term has no effect on the dimer or bulk properties predicted by the BOP parametrization. Expressions for these and additional electron constraining terms are summarized along with the model parameters in Appendix C.

The surface free energy  $\gamma$  as calculated by the BOP with the newly defined EC term is shown in Fig. 5 along with DFT surface free energy data from Lee *et al.*<sup>97</sup> and Ohno,<sup>107</sup> as combined in Ref. 100. In the combined surface free energy diagram, free energy values were shifted so that the  $\alpha 2(2 \times 4)$  surface reconstruction was at zero energy instead of the absolute values of  $\gamma_{\alpha 2(2 \times 4)}^{\text{BOP}} = 76.18 \text{ meV/\AA}^2$  and  $\gamma_{\alpha 2(2 \times 4)}^{\text{DFT}} = 43.38 \text{ meV/\AA}^2$  for the BOP and DFT, respectively.

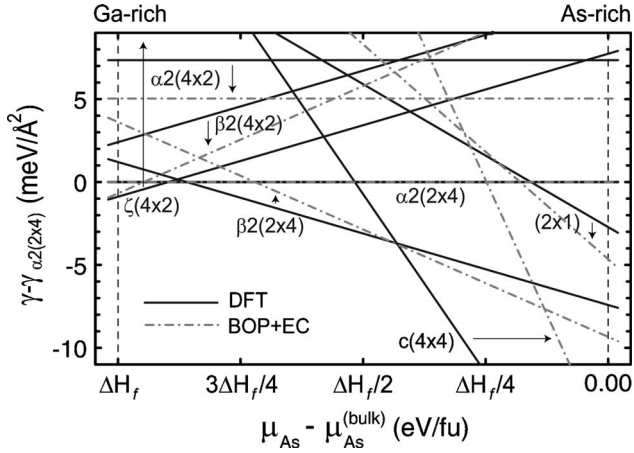


FIG. 5. GaAs (001) relative surface free energies predicted by DFT (Refs. 97 and 107) and the BOP+EC calculations for selected surface reconstructions. The arrows connect the DFT and BOP+EC results for the same surface. Surface free energies are plotted relative to the  $\alpha 2(2 \times 4)$  reconstruction and relative chemical potential values are scaled so that the heat of formation values overlap.

Additionally, since the DFT and BOP calculations have different heats of formation [ $\Delta H_f = -0.91$  eV/f.u. for BOP and  $-0.58$  eV/f.u. for GGA DFT (Ref. 97)] that bound the surface free diagram, the chemical potential data were scaled by  $|\Delta H_f|$  and plotted between 0 and a general  $\Delta H_f$  value.

From Fig. 5, it is clear that electron conservation introduced by the EC rule correctly destabilizes the appropriate reconstructions. These modified BOP+EC results are significantly better than the previous implementation of an EC energy penalty with empirical Stillinger-Weber and Tersoff formats.<sup>100</sup> Specifically, the BOP+EC potential predicted both the  $\beta(2 \times 4)$  and  $c(4 \times 4)$  surface reconstructions to be stable under arsenic-rich and very arsenic-rich conditions.

The charge buildup effects that destabilize the  $\beta(2 \times 4)$  surface reconstruction with respect to the  $\beta 2(2 \times 4)$  reconstruction were not included in the model due to the absence of Coulombic electrostatic interactions.<sup>93</sup> Therefore, the BOP surface free energy predictions cannot significantly differentiate between the  $\beta(2 \times 4)$  and  $\beta 2(2 \times 4)$  surface reconstructions. This represents an overstabilization of the  $\beta(2 \times 4)$  surface free energy by a small 2.2–3.1 meV/Å<sup>2</sup> margin as calculated by DFT.<sup>97,108</sup> The free energies of other structures that are not distinguishable include  $\gamma_{\beta(2 \times 4)} \approx \gamma_{\beta 2(2 \times 4)}$ ,  $\gamma_{\beta(4 \times 2)} \approx \gamma_{\beta 2(4 \times 2)}$ ,  $\gamma_{\alpha(2 \times 4)} \approx \gamma_{\alpha 2(2 \times 4)}$ , and  $\gamma_{\alpha(4 \times 2)} \approx \gamma_{\alpha 2(4 \times 2)}$ .

In Fig. 5, the surface free energies for the  $c(4 \times 4)$  and  $\beta 2(2 \times 4)$  reconstructions predicted by the BOP+EC are generally consistent with DFT calculations. However, the  $\zeta(4 \times 2)$  surface is much less stable for the BOP+EC [not shown, but an arrow is drawn toward it from the DFT  $\zeta(4 \times 2)$  free energy line]. Instead the  $\beta 2(4 \times 2)$  surface was found to be the most stable gallium-rich reconstruction. The choice of a simplified low-energy gallium structure in the BOP parametrization may explain why the much simpler  $\beta 2(4 \times 2)$  surface is preferred over the more complex  $\zeta(4 \times 2)$  reconstruction. Despite this simplification of the gallium-rich surface structure, the simulation of thin film

growth should not be adversely affected because arsenic-rich  $\beta(2 \times 4)$  and  $\beta 2(2 \times 4)$  surfaces are dominant during most epitaxial growth conditions (especially under high temperatures above 800 K).<sup>87</sup>

In addition to surface structure, molecular and surface bonding of arsenic dimers to gallium-rich surfaces also needs to be studied dynamically using MD to fully evaluate the potential. This is because even a carefully parametrized, widely successful GaAs Tersoff potential failed to predict arsenic dimer bonding to the (001) surface ( $\text{As}_2$  sticking ratio near zero).<sup>20,23</sup> However, due to the significant amount of data that were produced in the calculations of the condensation mechanisms, the surface interactions using the BOP will be discussed in an upcoming paper.<sup>109</sup>

#### IV. CONCLUSIONS

(i) A computationally efficient analytic bond-order potential has been derived from tight-binding theory in a manner that course grains and links the electron structure to the local atomic structure.

(ii) A two-level version of the BOP was parametrized for gallium, arsenic, and GaAs material systems using a two-step process that separately fit radial and angular dependences. Gallium bulk properties were simplified to take the lowest-energy fcc structure, instead of the more complex  $\alpha\text{Ga}$  phase. Similar simplifying choices for bulk moduli data, tetramer structure, and the zb  $c_{44}$  elastic constant were made during the parametrization. These approximations were traced back to the choice of the two-center approximation for bond integral and repulsive energy terms.

(iii) The BOP was evaluated by comparing the properties of small clusters, bulk atomic properties (atomic volume, cohesive energies, and elastic constants), simple point defects, and surface properties with other (experimental and DFT) estimates.

(iv) The potential most successfully modeled dimer, trimer, and bulk property trends. The deviations were generally within 15% of the atomic volume and 8% of the cohesive energy values predicted by *ab initio* methods. The bulk moduli calculated by the BOP were generally within 50% of values predicted by DFT, while the GaAs zb elastic constants were a good approximation of the DFT and experimental results. The melting temperature was predicted within 28% of experimentally measured temperature.

(v) Neutral point-defect formation energies were calculated for the BOP and compared to DFT data. The calculated formation energies and local configurations were generally consistent with DFT data. The arsenic and gallium antisite defects from the BOP most closely matched the DFT predictions. However, the local environments of the interstitial defects did deviate some from the DFT data.

(vi) The complexities of the polar GaAs (001) arsenic-rich surface reconstruction were captured by using a combination of the BOP and a newly developed electron counting potential. The gallium-rich lowest-energy surface reconstruction was simplified from the  $\zeta(4 \times 2)$  to the  $\beta(4 \times 2)$  reconstruction, which is consistent with the simplified approximation made for the gallium bulk phase.

## ACKNOWLEDGMENTS

We gratefully acknowledge the support of this work by DARPA and ONR under ONR Contract No. N00014-03-C-0288. C. Schwartz and J. Christodoulou are the program managers. D.N.M. would like to acknowledge cofunding from EPSRC and EURATOM.

## APPENDIX A: PARAMETRIZATION METHODS

The analytic bond-order potential can be used to predict the lattice constants, cohesive energy, and elastic constants of a large variety of phases. These can then be compared to experimental or *ab initio*-calculated values and the free parameters of the BOP fitted to match expected property estimates. At first glance, it would appear that a fitting method that sets the target values for desired properties, puts physical limits on parameters, and minimizes the sum of the square deviation of the predicted properties from the target values would lead to a good set of parameters for the potential. However, this is not the case because the target properties are reported as discrete values and do not usually form a continuous function as required by the choice of smooth two-body repulsive and bond integral terms. The values of these Goodwin-Skinner-Pettifor<sup>34</sup> two-body terms depend on the distance between the two atoms of the bond and are not influenced by the bonding environment. The choice to use this two-body format is a significant approximation<sup>55</sup>; however, a highly transferable potential can be developed providing characteristic material system trends are used in the free parameter fitting rather than raw target properties.

Albe *et al.*<sup>20</sup> discovered that for the Tersoff potential, the bond energy of cubic structures and dimers can be expressed only as a function of bond length. Because cohesive energies and lattice constants of a variety of cubic phases essentially define the trend of the bond energy versus bond length relation, this finding enabled Albe *et al.* to determine all the pair functions by requiring the predicted bond energy versus bond length relation to match the bonding trends defined by the target properties of cubic structures and dimers. Once the pair functions were fully determined using this method, the angular function parameters were optimized in a second step to best match additional gallium, arsenic, and GaAs properties. This approach significantly improved the transferability of the potential. The BOP has a similar characteristic that allowed determination of all the pair functions by matching the predicted bond energy versus bond length curve to the bonding trend defined by the target properties of a variety of simple structures, such as dimer, trimer, and cubic crystals. The crystallographic information for the crystal structures is included in Appendix B.

Using the equations in Sec. II A, the bond energy  $E_b$  as a function of interatomic spacing  $r$  can be written as

$$E_b = \phi_0 f^m(r) - 2\beta_{\sigma,0} f^n(r) \Theta_\sigma - 2\beta_{\pi,0} f^n(r) \Theta_\pi. \quad (\text{A1})$$

The  $m$  and  $n$  parameters help define the normalized potential hardness,  $(\phi'/\phi)/(\beta'/\beta)|_{r=r_0} = m/n$  ( $\beta_\sigma$  or  $\beta_\pi$  are equivalent for this calculation).<sup>110</sup> This quantity determines the shape of the energy curve by measuring the relative stiffness

of the repulsive energy curve ( $\phi$ ) compared with the attractive energy curves ( $\beta_\sigma$  and  $\beta_\pi$ ). For a hard-sphere potential, the normalized potential hardness is  $\infty$ , while for carbon  $m/n=2.2$  and for silicon  $m/n=1.8$ .<sup>110</sup> In this parametrization,  $m/n$  was targeted at 2.0 during the fitting process.

For structures that have only the first-nearest-neighbor (1NN) shell within the cutoff distance, the bond orders  $\Theta_\sigma$  and  $\Theta_\pi$  have a single value and remain constant during application of a hydrostatic strain. Such 1NN structures include dimer, trimer, and some tetramer structures for both elements and binary systems; diamond cubic (dc), simple cubic (sc), and face-centered cubic (fcc) elemental crystals; and zinc blende (zb) and the NaCl binary crystal structures. Additionally, the 1NN shell of the body-centered cubic (bcc) and CsCl phases can be included. The equilibrium bond energy as a function of equilibrium bond lengths for these structures was derived from Eq. (A1), using the equilibrium condition  $E'_b=0$ :

$$E_b = \left(1 - \frac{m}{n}\right) \phi_0 f^m(r). \quad (\text{A2})$$

Equation (A2) depends only on the GSP pair function and related parameters.

Using a similar approach, the bond energy curvature at the equilibrium bond length was derived as

$$E''_b = m^2(1 - n/m) \phi_0 f^{m-2}(r) [f'(r)]^2. \quad (\text{A3})$$

The curvature is simply related to the bulk modulus  $B$ :

$$B = \frac{ZE''_b}{18Fr}, \quad (\text{A4})$$

where  $Z$  is the atomic coordination in the solid (the cohesive energy per atom is  $ZE_b/2$ ) and  $F$  is defined as the prefactor in the atomic volume,  $V=Fr^3$ . The values of  $F$  are arbitrarily chosen as unity for dimer, trimer, and tetramer clusters and take the values of 1 for sc lattice,  $8\sqrt{3}/9$  for the dc lattice,  $\sqrt{2}/2$  for fcc, and  $4\sqrt{3}/9$  for bcc structures. The coordinations  $Z$  are 1, 2, 3, 4, 6, 8 (1NN shell), and 12 for dimer, trimer, tetrahedron, dc, sc, bcc, and fcc structures, respectively.

To ensure the potential energy functions do not have a large slope change at the junction between the GSP function and the spline cutoff distance ( $r_1$ ), the GSP term  $f^n$  of the bond integral terms is required to decay to a small number—that is,  $f^n(\alpha r_0) < \mathcal{T}$ , where  $\mathcal{T} \approx 0.1-0.2$  and  $\alpha \approx 1.5$ . The bond-integral GSP term was used because it has a longer interaction range than the repulsive term,  $f^m$ .

Equations (A2) and (A3) can be used to fit the target bond energy and bulk modulus for a variety of structures with different bond lengths under the  $f^n$  constraint to determine the  $\phi_0$ ,  $m$ ,  $n$ , and  $n_c$  parameters. The target values (gathered from density functional theory or DFT<sup>19-22</sup> and experimental sources<sup>18,50,52-54,56</sup>) and the fitted bond energy and bulk modulus GSP curves are shown in Fig. 6 as a function of equilibrium bond length for many gallium, arsenic, and GaAs phases. In Fig. 6, the experimental or *ab initio* data are marked by open triangles. Notice that many of the data points do not fall in a trend that allows the GSP curve to

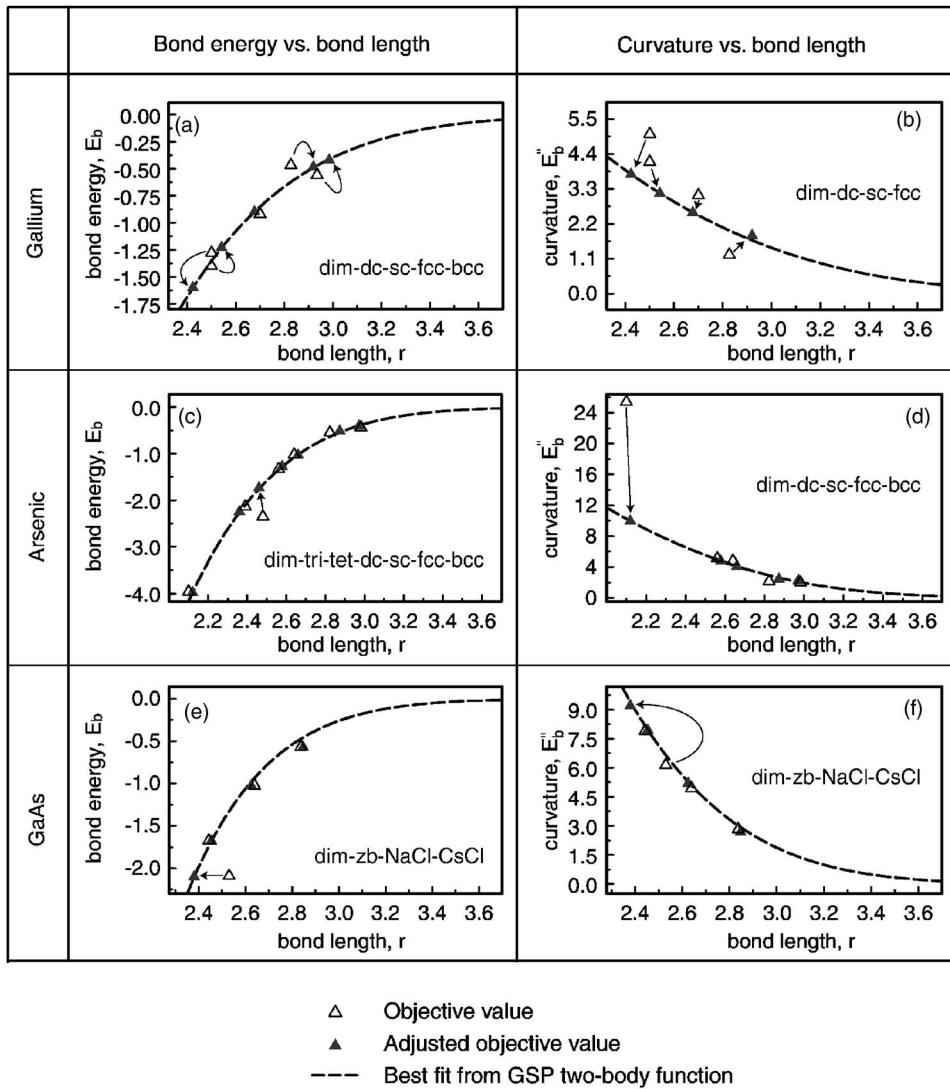


FIG. 6. Bond energy and curvature versus equilibrium bond length versus representing the best fit of the GSP-based two-body functions (dashed lines). The objective values ( $\Delta$ ) from experimental measurements and *ab initio* calculations are adjusted ( $\blacktriangle$ ) so that the GSP functional form can fit the data for the dimer (dim), trimer (tri), tetrahedral tetramer (tet), dc, zb, sc, NaCl, fcc, bcc (1NN shell), and CsCl (1NN shell) structures. The order of the structure for each system is shown in each panel.

intersect all the points. This makes the fitting process difficult, since all the original points cannot be intersected. Therefore, these initially predicted values were iteratively adjusted to fit GSP curves (see the arrows) that define smooth trends. The adjusted values are marked as solid triangles and were used as the target values in subsequent fittings. Numerous minimization routines, such as the downhill simplex method of Nelder and Mead,<sup>111</sup> a genetic algorithm, or biased random walk (simulated annealing),<sup>112</sup> were used to determine the parameters that minimize the mean-square difference between the target and predicted values.

From the equilibrium  $E'_b=0$ , the target bond-order values for the nearest-neighbor structures satisfy

$$\beta_{\sigma,0}\Theta_{\sigma} + \beta_{\pi,0}\Theta_{\pi} = \frac{m\phi_0 f^m(r)}{2n f^n(r)}. \quad (\text{A5})$$

Equation (A5) enables the  $\beta_{\sigma,0}$ ,  $\beta_{\pi,0}$ ,  $c_{\sigma}$ ,  $f_{\sigma}$ ,  $k_{\sigma}$ ,  $p_{\pi}$ ,  $p_{\sigma}$ , and  $b_{\sigma}$  parameters to be determined by fitting the bond orders for nearest-neighbor structures.

The fitting of remaining parameters for gallium utilized mainly the 1NN bond-order values generated using Eq. (A5). In addition, the bcc structure (including the second-nearest-

neighbor shell) was tested. The  $\alpha$ Ga (*A11,Cmca*) is the lowest-energy phase for gallium. The local atomic configuration around each atom in  $\alpha$ Ga is quite complex and has one neighbor within a covalent bonding radius and six atoms at metallic-like bonding distances.<sup>60</sup> After unfruitful efforts to try to force a fit of the  $\alpha$ Ga phase, we found that the BOP could not stabilize all seven bonds with their correct bond lengths. The fcc phase is predicted by DFT to be only 0.04–0.07 eV less stable than the  $\alpha$ Ga structure.<sup>20,21,113</sup> Therefore, we chose to approximate the low-energy gallium structure with the fcc structure. Other attempts to stabilize the  $\alpha$ Ga bonding environment with interatomic potentials that employ two-body repulsive and attractive bonding terms also failed.<sup>20,23</sup> However, one interatomic potential format did report some success with modeling the  $\alpha$ Ga structure by including a screening function.<sup>21</sup> It is therefore likely that screening bonding and repulsive interactions, by incorporation of the environmental dependence around each pair of bonds as well as the usual interatomic spacing, would aid in the modeling of the  $\alpha$ Ga crystalline structure.

Like gallium, arsenic bond-order parameters were fit using mainly the nearest-neighbor structures. However, the

TABLE VIII. The atomic volume  $V$ , cohesive energy  $E_c$ , unrelaxed bulk modulus  $B_0$ , and bulk modulus pressure derivative  $B'$  were calculated for the GaAs system using the BOP. The *Stukturbericht* designation and space group notation are provided for the less common structures.

Material	Structure	$V$ ( $\text{\AA}^3/\text{at}$ )	$E_c$ (eV/at)	$B_0$ (GPa)	$B'$
GaAs	zb	22.714	-3.370	75.1	3.8
	sc16 (-, $Pa\bar{3}$ )	20.862 <sup>a</sup>	-3.170	82.0	3.3
	CrB ( $B33$ , $Cmcm$ )	21.685 <sup>b</sup>	-3.103	105.5	3.1
	NaCl	18.078	-2.926	107.3	4.3
	NiAs	18.511	-2.875	109.9	4.3
	CsCl	16.396	-2.596	167.7	6.1
Ga	fcc	17.625	-2.838	84.2	3.7
	bcc	16.000	-2.769	160.6	3.4
	$\beta$ Ga ( $A20$ , $Cmcm$ ) <sup>d</sup>	18.232 <sup>e</sup>	-2.745	71.9	3.6
	bcc12/Ga-II (-, $I\bar{4}3d$ )	16.740	-2.602	105.2	4.7
	$\alpha$ Ga ( $A11$ , $Cmca$ )	21.003 <sup>f</sup>	-2.593	49.3	3.3
	sc	19.287	-2.585	49.1	3.2
	dc	25.317	-2.382	27.9	2.9
	As	$\alpha$ As ( $A7$ , $R\bar{3}m$ )	19.874 <sup>g</sup>	-2.990	82.0
arsenolamprite ( $A11$ , $Cmca$ )		19.821 <sup>h</sup>	-2.969	78.1	5.1
sc		19.303	-2.867	78.1	3.6
dc		26.644	-2.501	42.2	3.4
bcc		18.500	-2.340	103.9	3.9
graphite		24.706 <sup>i</sup>	-2.258	42.3	3.5
fcc		18.844	-2.256	101.7	4.6

<sup>a</sup> $u=0.151$ ,  $v=0.649$ .

<sup>b</sup> $a=4.341$ ,  $b=7.518$ ,  $c=5.316$ ,  $u=0.833$ ,  $v=0.167$ .

<sup>c</sup> $c/a=1.633$ .

<sup>d</sup> $\beta$ Ga has the monoclinic symmetry ( $C2/c$ ), but  $A20$ , an approximately similar structure (Ref. 21).

<sup>e</sup> $a=2.768$ ,  $b=9.157$ ,  $c=2.877$ ,  $u=0.132$ .

<sup>f</sup> $a=4.548$ ,  $b=7.484$ ,  $c=4.936$ ,  $u=0.162$ ,  $v=0.088$ .

<sup>g</sup> $c/a=2.965$ ,  $u=0.232$ .

<sup>h</sup> $a=5.407$ ,  $b=8.180$ ,  $c=3.585$ ,  $u=0.145$ ,  $v=0.250$ .

<sup>i</sup> $c/a=1.306$ .

structure and cohesive energy of the  $\alpha$ As ( $A7$ ,  $R\bar{3}m$ ) (Ref. 60) and arsenolamprite ( $A11$ ,  $Cmca$ ) (Ref. 114) phases were also evaluated within the iterative bond-order fitting process. Monitoring the arsenolamprite structure and binding energy during the selection process was critical to the successful prediction of the low-energy  $\alpha$ As phase.

At this point, the cutoff parameters ( $r_1$  and  $r_{\text{cut}}$ ) for the spline were arbitrarily set to give the longest interaction length within the first-nearest-neighbor shell. (For arsenic, this included both the first and second sets of three neighbors.) The value of  $r_{\text{cut}}$  was adjusted by hand at the end of the fitting process if a small change ( $<0.1$   $\text{\AA}$ ) was helpful in moving particular shells of atoms outside the interaction range.

For GaAs, the parameters for the bond order were fit using the nearest-neighbor structures, such as dimer, symmetric trimers (As-Ga-As or Ga-As-Ga), zb, and NaCl structures. Additionally, the cohesive energy for the CsCl (having both

nearest- and next-nearest-neighbor shells) and a simple cubic structure with 16 atoms in the unit cell (sc16,  $Pa\bar{3}$ ) (Ref. 115) were evaluated in the bond-order fitting process. It was necessary to monitor the energy of the sc16 structure during the fitting process because it can easily stabilize (with respect to the zb phase) with relatively small changes in the angular parameters ( $p_\sigma$  and  $b_\sigma$ ). The unrelaxed zb elastic constants ( $c'$  and  $c_{44}$ ) were fit; however, due to the fact that elastic constants were reasonably close ( $\pm 20\%$ ) without fitting, we found this constraint only helped refine the values.<sup>32,116,117</sup> The equilibrium bond angles and bond lengths of asymmetric trimers (e.g., As-Ga-Ga and As-As-Ga) from *ab initio* data<sup>22</sup> were used to assist the fitting of these angular parameters. These symmetric and asymmetric angular parameters also affected the unrelaxed vacancy and antisite defect formation energies, which were also used to help determine their values. Utilization of angular parameters that depended on the species type of all three atoms in the bond angle

proved very useful for predicting accurate defect formation energies.

After each fitting iteration, the best parameter set was tested for a large collection of bulk structures; see Appendix B. Providing no spurious structures were detected (for example, a structure is found to have a lower cohesive energy than the ground state phase), the properties outlined in Sec. III were evaluated. If a significant problem was identified during this evaluation, the entire process was repeated with the necessary adjustments.

## APPENDIX B: SUMMARY OF THE BOP CRYSTALLINE DATA

Not all the bulk crystalline structures evaluated in our analysis of the bond-order potential parametrization were reported in Fig. 3 due to the lack of consistent local density approximation density functional theory data. Therefore, additional bulk property information for a larger collection of structures has been summarized for gallium, arsenic, and GaAs structures in Table VIII.<sup>57,118</sup> The abbreviated crystal structure names are defined as zb (zinc blende), sh (simple hexagonal), sc (simple cubic), fcc (face-centered cubic), bcc (body-centered cubic), hcp (hexagonal close-packed), dc (diamond cubic), and fct (face-centered tetragonal).

In addition to its usefulness for reference, the additional structural information for arsenic in Table VIII showed that the arsenolamprite structure was 21 meV/atom less stable than the lowest-energy  $\alpha$ As phase. The arsenolamprite structure has been observed experimentally.<sup>114</sup> A variety of different metastable structural parameters were found for the arsenolamprite structure, with the one in Table VIII being the most stable. It is interesting to note that the arsenolamprite and  $\alpha$ As phases were very similar. The first-nearest-neighbor shell of these structures had identical bond lengths; however, for more distant neighboring shells, the  $\alpha$ As shells were generally split into multiple shells with different bond lengths in the arsenolamprite structure.

## APPENDIX C: ELECTRON COUNTING POTENTIAL

The electron counting potential enables atoms to redistribute their valence electrons among interatom bonds and dangling bonds at a surface to reduce the potential energy in  $E_{EC}$  within physical constraints as outlined by the EC rule.<sup>5,105</sup> The EC term can be directly added to the potential energy predicted by the bond-order potential in Eq. (1). Its form

$$U_{EC} = E_b + E_d + \sum_{n=1}^6 E_{c,n} \quad (C1)$$

is expressed as a sum of terms that controls the electron occupation of covalent bonds ( $E_b$ ) and dangling bonds ( $E_d$ ), along with a series of six physically motivated limits on the electron population ( $E_{c,1}-E_{c,6}$ ). The derivation and detailed explanation for these terms are discussed in Ref. 106. Here a brief summary of the format and parameters are discussed. The explicit expressions for these terms are all dependent on

the expressions and quantities that are summarized in Table IX.

The EC bond energy penalty  $E_b$  constrains the electron occupation of interatom bonds with

$$E_b = \sum_i \sum_{j,j \neq i} b_{ij} P_{ij}^2 \left( a_{ij} + a_{ji} - \frac{q_{ij}}{q_{0,ij}} - \frac{q_{ji}}{q_{0,ji}} \right)^2, \quad (C2)$$

where the coefficient  $b_{ij}$  determines the strength of the energy penalty,  $q_{ij}/q_{0,ij}$  is the normalized static electron distribution that depends on the  $ij$  bond length, and  $a_{ij} + a_{ji}$  is the dynamic electron distribution between atoms  $i$  and  $j$ . In addition,  $P_{ij}$  characterizes the nature of the bond between atoms  $i$  and  $j$ , so that  $P_{ij}=0$  indicates that the  $ij$  bond is in the bulk and  $P_{ij}=1$  signifies that  $ij$  is on the surface. The parameters  $b_{ij}$  and  $q_{0,ij}$  (along with  $r_{a,ij}$  and  $r_{c,ij}$  as used in  $q_{ij}$  in Table IX) are dependent on the types of atoms in the  $ij$  bond.

The EC dangling bond energy penalty  $E_d$  controls the electron occupation in dangling bonds using

$$E_d = \sum_i w_{d,i} (S_i Z_i)^2 (d_i n_i - \alpha_i n_i)^2, \quad (C3)$$

where  $w_{d,i}$  reflects the strength of the energy penalty for each atom  $i$ ,  $\alpha_i$  is the electron affinity of atom  $i$ ,  $n_i$  is the number of dangling bonds around atom  $i$ , and  $d_i n_i$  is the number of electrons donated from atom  $i$  to its dangling bonds; see Table IX. The low-coordination order function  $S_i$  has a high value ( $S_i=1$ ) for low-coordination environments and a low value ( $S_i=0$ ) for highly coordinated bulk environments. An additional high-coordination order function  $Z_i$  takes a value of  $Z_i=1$  for highly coordinated atoms and  $Z_i=0$  for low-coordinated atoms.

The boundaries on the electron distribution are physically limited by six constraining energy terms. The continuous redistribution of electrons in covalent bonds and dangling bonds is bounded between 0 (number must be positive) and 2 (Pauli exclusion principle). The energy constraints can be expressed for dangling bonds as  $0 \leq d_i n_i \leq 2n_i$ ,

$$E_{c,1} = \sum_i C(-d_i n_i), \quad (C4)$$

$$E_{c,2} = \sum_i C(d_i n_i - 2n_i), \quad (C5)$$

and for interatom bonds as  $0 \leq a_{ij} + a_{ji} \leq 2$ ,

$$E_{c,3} = \sum_i \sum_{j,j \neq i} C(-a_{ij} - a_{ji}), \quad (C6)$$

$$E_{c,4} = \sum_i \sum_{j,j \neq i} C(a_{ij} + a_{ji} - 2). \quad (C7)$$

Furthermore, the ability of atoms  $i$  and  $j$  to transfer electrons decays to zero as the interatomic distance  $r_{ij}$  is increased to the interaction cutoff distance  $r_{c,ij}$ . To ensure that energy and electron distributions are continuous during dynamic simulation, the  $\lambda_{ij} \leq g_{ij} \leq \mu_{ij}$  constrains the total number of electrons in the  $ij$  bond, as expressed by



TABLE IX. Expressions and quantities necessary for the calculation of the EC potential. The EC free parameters ( $V_i$ ,  $\alpha_i$ ,  $q_{0,ij}$ ,  $r_{a,ij}$ ,  $r_{c,ij}$ ,  $r_{s,ij}$ ,  $w_{d,i}$ ,  $b_{ij}$ , and  $w_c$ ) are summarized in Table X. The  $e^-$  is an abbreviation used below for “electron” or the “number of electrons.”

Function description	Equation
Dynamic $e^-$ distribution in bond	$a_{ij}$ =dynamically solved
Static $e^-$ distribution in bond	$q_{ij} = \begin{cases} q_{0,ij}, & r_{ij} \leq r_{a,ij} \\ q_{0,ij} \frac{(3r_{a,ij} - r_{c,ij} - 2r_{ij})(r_{ij} - r_{c,ij})^2}{(r_{a,ij} - r_{c,ij})^3}, & r_{a,ij} < r_{ij} < r_{c,ij} \\ 0, & r_{c,ij} \leq r_{ij} \end{cases}$
Bulk coordination around atom	$\nu_i=4$ (fixed for tetrahedral structures)
Bonding fraction for atom	$F_{0,i} = \sum_{j,j \neq i} q_{ij}(r_{ij}) / V_i$
Overbonding correction for atom	$\Delta F_i = \begin{cases} 0, & F_{0,i} \leq 1 \\ F_{0,i} - 1, & F_{0,i} > 1 \end{cases}$
Corrected fractional bonding for atom	$F_i = F_{0,i} - \Delta F_i$
General order function	$G(x, x_s, x_f) = \begin{cases} 0, & x \leq x_s \\ \frac{1}{2} - \frac{1}{2} \cos\left(\pi \frac{x - x_s}{x_f - x_s}\right), & x_s < x < x_f \\ 1, & x_f \leq x \end{cases}$
Surface coordination order	$P_{ij} = G(n_{m,ij}, 0.50, 0.75)$
Low-coordination order	$S_i = G(n_{0,i}, 0.25, 0.50)$
High-coordination order	$Z_i = G(F_i, 0.26, 0.40)$
Dangling bonds around atom	$n_i = \nu_i(1 - F_i)$
$e^-$ from atom $i$ in dangling bonds	$d_i n_i = V_i - \sum_j g_{ij}$
$e^-$ from atom $i$ in bond	$g_{ij} = P_{ij} a_{ij} + (1 - P_{ij}) \frac{q_{ij}}{1 + \Delta F_i}$
Lower limit of $e^-$ from atom $i$ in bond	$\lambda_{ij} = \max(V_i - 2\nu_i, 2 - V_j) q_{ij} / q_{0,ij}$
Upper limit of $e^-$ from atom $i$ in bond	$\mu_{ij} = \min(V_i, 2 + 2\nu_j - V_j) q_{ij} / q_{0,ij}$
Rescaled $n_i$	$n_{0,i} = n_i$ , with nearest-neighbor distance rescaled to $r_{s,ij}$ <sup>a</sup>
Environmental parameter for atom	$n_{m,i} = \max [n_{0,k} q_{ik} / q_{0,ik}, \text{ with } k = 1, 2, \dots, N]$
Environmental parameter for bond	$n_{m,ij} = \max [\min(n_{m,i}, n_{m,j}), n_{0,i}, n_{0,j}]$
General constraint function	$C(x) = \begin{cases} 0, & x < 0 \\ w_c x^2, & x \geq 0 \end{cases}$

<sup>a</sup>Rescaling can be omitted to improve calculation speed, assuming the crystal is not significantly stretched.

$$E_{c,5} = \sum_i \sum_{j,j \neq i} C(\lambda_{ij} - g_{ij}), \quad (\text{C8})$$

$$E_{c,6} = \sum_i \sum_{j,j \neq i} C(g_{ij} - \mu_{ij}). \quad (\text{C9})$$

These terms have no effect on  $g_{ij}$  at small bond lengths but force the value to zero as the bond length approaches the cutoff,  $r_{c,ij}$ .

The EC term required the material-specific atomic valence ( $V_i$ ) and electron affinity ( $\alpha_i$ ) parameters, the bond-dependent static electron distribution parameters ( $q_{0,ij}$ ,  $r_{a,ij}$ , and  $r_{c,ij}$ ), rescaling radius for the  $ij$  bond ( $r_{s,ij}$ ) used in the calculation of  $n_{0,i}$ , the dangling bond and bonding energy penalty coefficients ( $w_{d,i}$  and  $b_{ij}$ ), and the electron population constraint coefficient ( $w_c$ ) to be determined. The static electron distribution parameters were previously reported,<sup>106</sup> the  $r_s$  values were chosen from the values of  $r_0$  used in the BOP,

TABLE X. EC potential parameters. The parameters for keeping the electron occupation within appropriate bounds are set at  $w_c = 100.0$  eV.

Symbol	Quantity	Ga-Ga	As-As	Ga-As
$V_i$	Atomic valence ( $e^-$ )	3.000	5.000	-
$\alpha_i$	Electron affinity ( $e^-$ )	0.000	2.000	-
$q_{0,ij}$	Static electron distribution ( $e^-/\text{bond}$ )	0.750	1.250	- <sup>a</sup>
$r_{a,ij}$	Static electron distribution, begin cutoff (Å)	2.600	2.800	2.700
$r_{c,ij}$	Static electron distribution, final cutoff (Å)	2.918	3.500	3.220
$w_{d,i}$	Dangling bond coeff. (eV/ $e^-$ )	1.836	1.836	-
$b_{ij}$	Bonding coeff. (eV/ $e^-$ )	4.450	4.450	4.450
$r_{S,ij}$	Rescaling radius (Å)	2.424	2.120	2.380

<sup>a</sup>Central atom ( $i$ ) specific parameter,  $q_{0,ij} = V_i/4$ —that is,  $q_{0,\text{GaAs}} = 0.750$  and  $q_{0,\text{AsGa}} = 1.250$ .

the  $w_d$  and  $b$  parameters were parametrized following the Appendix in Ref. 106, and  $w_c$  was arbitrarily chosen and fixed for all atomic and bonding environments. The ECP parameters are summarized in Table X.

The EC potential energy ( $U_{\text{EC}}$ ) has been expressed as a function of atom positions and the dynamic electron population,  $a_{ij}$  and  $a_{ji}$ . For any set of atomic positions, the dynamic electron population can be solved from the equilibrium (minimum energy) conditions using the conjugate gradient method coupled with a Newton-Raphson algorithm.<sup>16</sup> Addi-

tionally, the EC potential can be calculated at each time step (or set of time steps) during full MD simulation. The dynamic electron population and EC energy penalty are continuous functions with respect to atom motion. Therefore, the efficiency of the calculations is significantly improved when the solutions for  $a_{ij}$  and  $a_{ji}$  are retained for the initial values in the next time step. Furthermore, it should be noted that because  $\partial E / \partial a_{ij} = 0$ , all derivatives of  $a_{ij}$  with respect to atom positions have no impact on the forces and stresses of the BOP.

\*Author to whom correspondence should be addressed. Electronic address: murdick@mailaps.org

<sup>1</sup>*Properties of Gallium Arsenide*, 3rd ed., edited by M. R. Brozel and G. E. Stillman, Vol. 16 of *EMIS Datareviews Series* (INSPEC, London, 1996).

<sup>2</sup>J. R. Arthur, *Surf. Sci.* **43**, 449 (1974).

<sup>3</sup>C. T. Foxon and B. A. Joyce, *Surf. Sci.* **64**, 293 (1977).

<sup>4</sup>J. M. Van Hove and P. I. Cohen, *Appl. Phys. Lett.* **47**, 726 (1985).

<sup>5</sup>J. P. Harbison and H. H. Farrell, *J. Vac. Sci. Technol. B* **6**, 733 (1988).

<sup>6</sup>G. R. Bell, T. S. Jones, and B. A. Joyce, *Surf. Sci.* **429**, L492 (1999).

<sup>7</sup>M. Itoh, G. R. Bell, A. R. Avery, T. S. Jones, B. A. Joyce, and D. D. Vvedensky, *Phys. Rev. Lett.* **81**, 633 (1998).

<sup>8</sup>M. Itoh, *Prog. Surf. Sci.* **66**, 53 (2001).

<sup>9</sup>M. Missous and S. O'Hagan, *J. Appl. Phys.* **75**, 3396 (1994).

<sup>10</sup>C. G. Morgan, P. Kratzer, and M. Scheffler, *Phys. Rev. Lett.* **82**, 4886 (1999).

<sup>11</sup>P. Kratzer, E. Penev, and M. Scheffler, *Appl. Surf. Sci.* **216**, 436 (2003).

<sup>12</sup>D. A. Murdick, X. W. Zhou, and H. N. G. Wadley, *J. Cryst. Growth* **286**, 197 (2006).

<sup>13</sup>E. T. Gawlinski and J. D. Gunton, *Phys. Rev. B* **36**, 4774 (1987).

<sup>14</sup>H. N. G. Wadley, X. Zhou, R. A. Johnson, and M. Neurock, *Prog. Mater. Sci.* **46**, 329 (2001).

<sup>15</sup>K. Shintani, T. Nakajima, and S. Kameoka, *J. Appl. Phys.* **95**, 446 (2004).

<sup>16</sup>X. W. Zhou, H. N. G. Wadley, J.-S. Filhol, and M. N. Neurock, *Phys. Rev. B* **69**, 035402 (2004).

<sup>17</sup>*Smithells Metals Reference Book*, 7th ed., edited by E. A. Brandes and G. B. Brook (Butterworth-Heinemann, Oxford, 1998).

<sup>18</sup>*CRC Handbook of Chemistry and Physics*, 83rd ed., edited by D. R. Lide (CRC Press, Boca Raton, FL, 2003).

<sup>19</sup>A. Mujica, R. J. Needs, and A. Munoz, *Phys. Rev. B* **52**, 8881 (1995).

<sup>20</sup>K. Albe, K. Nordlund, J. Nord, and A. Kuronen, *Phys. Rev. B* **66**, 035205 (2002).

<sup>21</sup>M. I. Baskes, S. P. Chen, and F. J. Cherne, *Phys. Rev. B* **66**, 104107 (2002).

<sup>22</sup>J. J. BelBruno, *Heteroat. Chem.* **14**, 189 (2003).

<sup>23</sup>D. A. Murdick, X. W. Zhou, and H. N. G. Wadley, *Phys. Rev. B* **72**, 205340 (2005).

<sup>24</sup>D. G. Pettifor, *Phys. Rev. Lett.* **63**, 2480 (1989).

<sup>25</sup>D. G. Pettifor and I. I. Oleinik, *Phys. Rev. B* **59**, 8487 (1999).

<sup>26</sup>D. G. Pettifor and I. I. Oleinik, *Phys. Rev. Lett.* **84**, 4124 (2000).

<sup>27</sup>D. G. Pettifor and I. I. Oleinik, *Phys. Rev. B* **65**, 172103 (2002).

<sup>28</sup>D. G. Pettifor, M. W. Finnis, D. Nguyen-Manh, D. A. Murdick, X. W. Zhou, and H. N. G. Wadley, *Mater. Sci. Eng., A* **365**, 2 (2004).

<sup>29</sup>R. Drautz, D. A. Murdick, D. Nguyen-Manh, X. W. Zhou, H. N. G. Wadley, and D. G. Pettifor, *Phys. Rev. B* **72**, 144105 (2005).

<sup>30</sup>D. G. Pettifor, *Bonding and Structure of Molecules and Solids*, Oxford Science Publications (Oxford University Press, Oxford, 1995).

<sup>31</sup>D. G. Pettifor, *Springer Proc. Phys.* **48**, 64 (1990).

<sup>32</sup>M. Finnis, *Interatomic Forces in Condensed Matter*, Oxford Series on Materials Modelling (Oxford University Press, Oxford, 2003).

- <sup>33</sup>A. P. Horsfield, A. M. Bratkovsky, M. Fearn, D. G. Pettifor, and M. Aoki, *Phys. Rev. B* **53**, 12694 (1996).
- <sup>34</sup>L. Goodwin, A. J. Skinner, and D. G. Pettifor, *Europhys. Lett.* **9**, 701 (1989).
- <sup>35</sup>C. Lanczos, *J. Res. Natl. Bur. Stand.* **45**, 225 (1950).
- <sup>36</sup>R. Haydock, *Solid State Phys.* **35**, 216 (1980).
- <sup>37</sup>R. Jones and M. W. Lewis, *Philos. Mag. B* **49**, 95 (1984).
- <sup>38</sup>J. Inoue and Y. Ohta, *J. Phys. C* **20**, 1947 (1987).
- <sup>39</sup>F. Cyrot-Lackmann, *Adv. Phys.* **16**, 393 (1967).
- <sup>40</sup>K. Ohno, K. Esfarjani, and Y. Kawazoe, *Computational Materials Science: From ab initio to Monte Carlo methods*, Vol. 129 of *Springer Series in Solid State Sciences* (Springer-Verlag, New York, 1999).
- <sup>41</sup>L. D. Landau and E. M. Lifshitz, *Mechanics*, 3rd ed. (Pergamon Press, New York, 1976).
- <sup>42</sup>A. Nordsieck, *Math. Comput.* **16**, 22 (1962).
- <sup>43</sup>C. H. Xu, C. Z. Wang, C. T. Chan, and K. M. Ho, *J. Phys.: Condens. Matter* **4**, 6047 (1992).
- <sup>44</sup>L. F. Mattheiss, D. R. Hamann, and W. Weber, *Phys. Rev. B* **34**, 2190 (1986).
- <sup>45</sup>X. Gonze, J.-P. Michenaud, and J.-P. Vigneron, *Phys. Rev. B* **41**, 11827 (1990).
- <sup>46</sup>M. Parrinello and A. Rahman, *J. Chem. Phys.* **76**, 2662 (1982).
- <sup>47</sup>J. R. Ray and A. Rahman, *J. Chem. Phys.* **80**, 4423 (1984).
- <sup>48</sup>Wolfram Research, Inc., *Mathematica*, version 5.1 ed. (Wolfram Research, Inc., Champaign, IL, 2004).
- <sup>49</sup>E. S. Tok, J. H. Neave, J. Zhang, B. A. Joyce, and T. S. Jones, *Surf. Sci.* **374**, 397 (1997).
- <sup>50</sup>K. P. Huber and G. Herzberg, *Molecular Spectra and Molecular Structure: IV. Constants of diatomic molecules* (Van Nostrand Reinhold Company, New York, 1979), Vol. 4.
- <sup>51</sup>L.-S. Wang, Y. T. Lee, D. A. Shirley, K. Balasubramanian, and P. Feng, *J. Chem. Phys.* **93**, 6310 (1990).
- <sup>52</sup>S. L. Bennett, J. L. Margrave, J. L. Franklin, and J. E. Hudson, *J. Chem. Phys.* **59**, 5814 (1973).
- <sup>53</sup>J. J. Murray, C. Pupp, and R. F. Pottier, *J. Chem. Phys.* **58**, 2569 (1973).
- <sup>54</sup>G. W. Lemire, G. A. Bishea, S. A. Heidecke, and M. D. Morse, *J. Chem. Phys.* **92**, 121 (1990).
- <sup>55</sup>D. Nguyen-Manh, D. G. Pettifor, and V. Vitek, *Phys. Rev. Lett.* **85**, 4136 (2000).
- <sup>56</sup>L. Brewer, Lawrence Berkeley Laboratory Report No. LBL-3720 (unpublished), 1977.
- <sup>57</sup>*Pearson's Handbook of Crystallographic Data for Intermetallic Phases*, 2nd ed., edited by P. Villars and L. D. Calvert (ASM International, Materials Park, Ohio, 1991), Vol. 1, pp. 1134–1135.
- <sup>58</sup>S. Adachi, in *Properties of Gallium Arsenide*, 3rd ed., edited by M. R. Brozel and G. E. Stillman (INSPEC, London, 1996), Vol. 16, pp. 27–31.
- <sup>59</sup>H. J. McSkimin, A. Jayaraman, and P. Andreatch, Jr., *J. Appl. Phys.* **38**, 2362 (1967).
- <sup>60</sup>J. Donohue, *The Structures of the Elements* (Wiley, New York, 1974).
- <sup>61</sup>K. R. Lyall and J. F. Cochran, *Can. J. Phys.* **49**, 1074 (1971).
- <sup>62</sup>H. J. Beister, K. Strössner, and K. Syassen, *Phys. Rev. B* **41**, 5535 (1990).
- <sup>63</sup>G. Kresse and J. Hafner, *J. Phys.: Condens. Matter* **6**, 8245 (1994).
- <sup>64</sup>G. Kresse and J. Hafner, *Phys. Rev. B* **47**, R558 (1993).
- <sup>65</sup>G. Kresse and J. Hafner, *Phys. Rev. B* **49**, 14251 (1994).
- <sup>66</sup>G. Kresse and J. Furthmüller, *Comput. Mater. Sci.* **6**, 15 (1996).
- <sup>67</sup>G. Kresse and J. Furthmüller, *Phys. Rev. B* **54**, 11169 (1996).
- <sup>68</sup>O. H. Nielsen and R. M. Martin, *Phys. Rev. B* **32**, 3792 (1985).
- <sup>69</sup>D. Nguyen-Manh, D. G. Pettifor, S. Znam, and V. Vitek, in *Tight-Binding Approach to Computational Materials Science*, edited by P. E. A. Turchi, A. Gonis, and L. Colombo, MRS Sympia Proceedings No. 491 (Materials Research Society, Warrendale, PA, 1998), pp. 353–358.
- <sup>70</sup>S. Znam, D. Nguyen-Manh, D. G. Pettifor, and V. Vitek, *Philos. Mag.* **83**, 415 (2003).
- <sup>71</sup>J. R. Morris, C. Z. Wang, K. M. Ho, and C. T. Chan, *Phys. Rev. B* **49**, 3109 (1994).
- <sup>72</sup>H. Wenzl, A. Dahlen, A. Fattah, S. Petersen, K. Mika, and D. Henkel, *J. Cryst. Growth* **109**, 191 (1991).
- <sup>73</sup>M. Ishimaru, K. Yoshida, and T. Motooka, *Phys. Rev. B* **53**, 7176 (1996).
- <sup>74</sup>G. Zollo, J. Tarus, and R. M. Nieminen, *J. Phys.: Condens. Matter* **16**, 3923 (2004).
- <sup>75</sup>D. C. Look, in *Properties of Gallium Arsenide*, 3rd ed., edited by M. R. Brozel and G. E. Stillman (INSPEC, London, 1996), Vol. 16, pp. 684–688.
- <sup>76</sup>J. I. Landman, C. G. Morgan, J. T. Schick, P. Papoulias, and A. Kumar, *Phys. Rev. B* **55**, 15581 (1997).
- <sup>77</sup>S. B. Zhang and J. E. Northrup, *Phys. Rev. Lett.* **67**, 2339 (1991).
- <sup>78</sup>J. E. Northrup and S. B. Zhang, *Phys. Rev. B* **47**, R6791 (1993).
- <sup>79</sup>G.-X. Qian, R. M. Martin, and D. J. Chadi, *Phys. Rev. B* **38**, 7649 (1988).
- <sup>80</sup>G. Zollo and R. M. Nieminen, *J. Phys.: Condens. Matter* **15**, 843 (2003).
- <sup>81</sup>D. J. Chadi, *Phys. Rev. B* **46**, 9400 (1992).
- <sup>82</sup>W. H. Press, *Numerical Recipes in Fortran 77: The art of scientific computing*, 2nd ed. (Cambridge University Press, New York, 1996), Vol. 1.
- <sup>83</sup>J. Tersoff, *Phys. Rev. B* **39**, R5566 (1989).
- <sup>84</sup>F. H. Stillinger and T. A. Weber, *Phys. Rev. B* **31**, 5262 (1985).
- <sup>85</sup>M. Sayed, J. H. Jefferson, A. B. Walker, and A. G. Cullis, *Nucl. Instrum. Methods B* **102**, 218 (1995).
- <sup>86</sup>M. J. Cawkwell, D. Nguyen-Manh, D. G. Pettifor, and V. Vitek, *Phys. Rev. B* (to be published).
- <sup>87</sup>Q.-K. Xue, T. Hashizume, and T. Sakurai, *Appl. Surf. Sci.* **141**, 244 (1999).
- <sup>88</sup>D. Paget, O. Pulci, M. Sauvage, Y. Garreau, L. Reining, P. Chiaradia, F. Bechstedt, and R. Pinchaux, *Surf. Rev. Lett.* **9**, 1497 (2002).
- <sup>89</sup>M. Pristovsek, S. Tsukamoto, A. Ohtake, N. Koguchi, B. G. Orr, W. G. Schmidt, and J. Bernholc, *Phys. Status Solidi B* **240**, 91 (2003).
- <sup>90</sup>S. Tsukamoto, M. Pristovsek, A. Ohtake, B. G. Orr, G. R. Bell, T. Ohno, and N. Koguchi, *J. Cryst. Growth* **251**, 46 (2003).
- <sup>91</sup>D. J. Chadi, *J. Vac. Sci. Technol. A* **5**, 834 (1987).
- <sup>92</sup>J. E. Northrup and S. Froyen, *Phys. Rev. Lett.* **71**, 2276 (1993).
- <sup>93</sup>J. E. Northrup and S. Froyen, *Phys. Rev. B* **50**, R2015 (1994).
- <sup>94</sup>P. Laukkanen *et al.*, *Phys. Rev. B* **72**, 045321 (2005).
- <sup>95</sup>D. K. Biegelsen, R. D. Bringans, J. E. Northrup, and L. E. Swartz, *Phys. Rev. B* **41**, 5701 (1990).
- <sup>96</sup>A. Ohtake and N. Koguchi, *Appl. Phys. Lett.* **83**, 5193 (2003).
- <sup>97</sup>S.-H. Lee, W. Moritz, and M. Scheffler, *Phys. Rev. Lett.* **85**, 3890 (2000).
- <sup>98</sup>Q.-K. Xue, T. Hashizume, and T. Sakurai, *Prog. Surf. Sci.* **56**, 1

- (1997).
- <sup>99</sup>K. Reuter and M. Scheffler, *Phys. Rev. B* **65**, 035406 (2001).
- <sup>100</sup>D. A. Murdick, X. W. Zhou, H. N. G. Wadley, and D. Nguyen-Manh, *J. Phys.: Condens. Matter* **17**, 6123 (2005).
- <sup>101</sup>M. A. Salmi, M. Alatalo, T. Ala-Nissila, and R. M. Nieminen, *Surf. Sci.* **425**, 31 (1999).
- <sup>102</sup>N. Moll, A. Kley, E. Pehlke, and M. Scheffler, *Phys. Rev. B* **54**, 8844 (1996).
- <sup>103</sup>M. Missous, in *Properties of Gallium Arsenide*, 3rd ed., edited by M. R. Brozel and G. E. Stillman (INSPEC, London, 1996), Vol. 16, pp. 679–683.
- <sup>104</sup>W. A. Harrison, *J. Vac. Sci. Technol.* **16**, 1492 (1979).
- <sup>105</sup>M. D. Pashley, *Phys. Rev. B* **40**, 10481 (1989).
- <sup>106</sup>X. W. Zhou, D. A. Murdick, and H. N. G. Wadley, *J. Appl. Phys.* (to be published).
- <sup>107</sup>T. Ohno, *Thin Solid Films* **272**, 331 (1996).
- <sup>108</sup>C. Sgiarovello, N. Binggeli, and A. Baldereschi, *Phys. Rev. B* **69**, 035320 (2004).
- <sup>109</sup>D. A. Murdick, X. W. Zhou, and H. N. G. Wadley (unpublished).
- <sup>110</sup>D. G. Pettifor, *Bonding and Structure of Molecules and Solids* (Oxford University Press, Oxford, 1995), pp. 77–81.
- <sup>111</sup>W. H. Press, *Numerical Recipes in Fortran 77: The art of scientific computing*, 2nd ed. (Cambridge University Press, New York, 1996), Vol. 1, pp. 402–406.
- <sup>112</sup>S. Wolfram, *The Mathematica Book*, 5th ed. (Wolfram Research, Inc., Champaign, IL, 2004), p. 106ff.
- <sup>113</sup>M. Bernasconi, G. L. Chiarotti, and E. Tosatti, *Phys. Rev. B* **52**, 9988 (1995).
- <sup>114</sup>W. L. Roberts, T. J. Campbell, and G. R. Rapp, *Encyclopedia of Minerals*, 2nd ed. (Van Nostrand Reinhold, New York, 1990).
- <sup>115</sup>M. I. McMahon, R. J. Nelmes, D. R. Allan, S. A. Belmonte, and T. Bovornratanaraks, *Phys. Rev. Lett.* **80**, 5564 (1998).
- <sup>116</sup>J. F. Nye, *Physical Properties of Crystals: Their representation by tensors and matrices*, Oxford Science Publications (Oxford University Press, Oxford, 1985).
- <sup>117</sup>A. Kelly and G. W. Groves, *Crystallography and Crystal Defects* (Longman, London, 1973).
- <sup>118</sup>J. L. C. Daams, P. Villars, and J. H. N. van Vucht, eds., *Atlas of Crystal Structure Types for Intermetallic Phases*, 2nd ed. (ASM International, Materials Park, Ohio, 1991), Vol. 1–4.